

Analysis Note: Identified particle flow measurements in Au+Au collisions at $\sqrt{s_{NN}} = 3$ GeV from RHIC-STAR*

Abstract

Collectivity is a powerful tool for understanding the properties of the medium created in high-energy nuclear collisions. In this letter we report the rapidity(y) dependence of azimuthally anisotropic parameters (v_1 and v_2) for identified hadrons ($\pi^\pm, K^\pm, K_S^0, p, \phi, \Lambda$) from Au+Au collisions at a center-of-mass-energy per nucleon pair ($\sqrt{s_{NN}}$) of 3 GeV. These results are compared with that from high collision energy $\sqrt{s_{NN}} > 4.5$ GeV. It is found that at this energy in the 10-40% mid-central collisions (1) the midrapidity slopes $dv_1/dy|_{y=0}$ for all hadrons are positive except pions; (2) the midrapidity elliptic flow v_2 are all negative and the number of consistent quark scaling, observed in high energy collision is absent. These observations imply new medium properties produced that are different from the partonic matter created in high energy collisions.

* shaoweilan@mails.ccnu.edu.cn

CONTENTS

List of Figures	3
List of Tables	7
1Analysis Setup	8
1Fixed Target Conventions	8
1Datasets and Event Selection cuts	8
1Badruns selection	9
1Centrality Determination	10
2Analysis Detail	11
2Event Plane Reconstruction	11
2TPC Event Plane Reconstruction	12
2EPPD Event Plane Reconstruction	13
2 ϕ -centering and shift calibration	14
2Event Plane Resolution	16
2Particle Identification	19
2PID from TPC and TOF	19
2Acceptance of pion, kaon and proton	20
2Purity	21
2Efficiency Correction	21
2TPC tracking efficiency	21
3Results	24
3v1.results for π, K, p	24
3plots v_1 as a function of p_T and rapidity	24
3krons' v_1 as a function of p_T and rapidity	28
3proton v_1 as a function of p_T and rapidity	31
3v2.results for π, K, p	35
3plots v_2 as a function of p_T and rapidity	35
3krons' v_2 as a function of p_T and rapidity	37
3proton v_2 as a function of p_T and rapidity	39

3v3.from second order event plane	41
3Systematic Uncertainties	45
4Discussion	52
4Number of constituent quark scaling of elliptic flow (v_2)	52

LIST OF FIGURES

1 These variables' (Vz, Vr, refmult, dca, eta, phi, pt) mean value as a function of run index.	9
2 The schematic plot of TPC and EPD sub-events	11
3 The schematic plot of EPD and EPD sub-events	13
4	14
5 TPC and EPD sub-event Ψ_1 distribution in different centrality, the black line is without raw Ψ_1 distribution, the blue line is with re-centering calibration, the red line is with re-centering and shift calibration	16
6 TPC and EPD sub-event event plane angle (Ψ_1) correlation	16
7 The event plane resolution for the n^{th} (n=km) harmonic of the particle distribution with respect to the m^{th} harmonic plane, as a function of v_m/σ .	17
8 EPD First order event plane resolution as a function of centrality for different sub-event groups. Different symbol means the same interest event plane resolution using different reference event plane.	19
9 Left: Energy loss dE/dx as a function of rigidity (p/q) for Au+Au collisions at $\sqrt{s_{NN}} = 3$ GeV. The dash lines indicate the theoretical predicated values for different particles. Right: $Mass^2$ as a function of rigidity (p/q) for Au+Au collisions at $\sqrt{s_{NN}} = 3$ GeV. The dash lines indicate the corresponding particles.	20
10 Rapidity(y) and transverse momentum(p_T) acceptance of $\pi^\pm, K^\pm, proton$ using TPC and TOF in Au+Au collisions at $\sqrt{s_{NN}} = 3$ GeV. The target is located at the $y = -1.045$.	22
11 pion TPC tracking efficiency as a function of p_T and rapidity for two-dimensional and separately.	22

12	K^+ TPC tracking efficiency as a function of p_T and rapidity for two-dimensional and separately.	23
13	K^- TPC tracking efficiency as a function of p_T and rapidity for two-dimensional and separately.	23
14	proton TPC tracking efficiency as a function of p_T and rapidity for two-dimensional and separately.	23
15	v_1 as a function of rapidity(y) in different centrality bins for π^+ and π^- in Au+Au collisions at $\sqrt{s_{NN}}$. The red line is fitting function.	25
16	pions' v_1 slope dv_1/dy as a function of centrality, (left) π^+ (right) π^- in Au+Au collisions $\sqrt{s_{NN}} = 3\text{GeV}$	26
17	pions' v_1 as a function of rapidity(y) in Au+Au collision at $\sqrt{s_{NN}}=3\text{GeV}$ in 0-10%, 10-40% and 40-60% bins.	26
18	pions' v_1 as a function of transverse momentum (p_T) in Au+Au collisions at $\sqrt{s_{NN}} = 3 \text{ GeV}$	27
19	pions' v_1 as a function of transverse momentum (p_T) in Au+Au collisions at $\sqrt{s_{NN}} = 3 \text{ GeV}$ in 0-10%, 10-40% and 40-60% centrality bins.	27
20	v_1 as a function of rapidity(y) in different centrality bins for K^+ and K^- in Au+Au collisions at $\sqrt{s_{NN}}$. The red line is fitting function.	28
21	kaons' v_1 slope dv_1/dy as a function of centrality, (left) K^+ (right) K^- in Au+Au collisions $\sqrt{s_{NN}} = 3\text{GeV}$	29
22	kaons' v_1 as a function of rapidity(y) in Au+Au collision at $\sqrt{s_{NN}}=3\text{GeV}$ in 0-10%, 10-40% and 40-60% bins.	29
23	kaons' v_1 as a function of transverse momentum (p_T) in Au+Au collisions at $\sqrt{s_{NN}} = 3 \text{ GeV}$	30
24	kaons' v_1 as a function of transverse momentum (p_T) in Au+Au collisions at $\sqrt{s_{NN}} = 3 \text{ GeV}$ in 0-10%, 10-40% and 40-60% centrality bins.	30
25	v_1 as a function of rapidity(y) in different centrality bins for proton in Au+Au collisions at $\sqrt{s_{NN}}$. The red line is fitting function.	31
26	protons' v_1 slope dv_1/dy as a function of centrality in Au+Au collisions $\sqrt{s_{NN}} = 3\text{GeV}$	32
27	protons' v_1 as a function of rapidity(y) in Au+Au collision at $\sqrt{s_{NN}}=3\text{GeV}$ in 0-10%, 10-40% and 40-60% bins.	32

28	protons' v_1 as a function of transverse momentum (p_T) in Au+Au collisions at $\sqrt{s_{NN}} = 3 \text{ GeV}$	33
29	protons' v_1 as a function of transverse momentum (p_T) in Au+Au collisions at $\sqrt{s_{NN}} = 3 \text{ GeV}$ in 0-10%, 10-40% and 40-60% centrality bins.	33
30	protons' v_1 as a function of p_T in fine rapidity bins and as a function of rapidity in fine p_T bins in 0-10%, 10-40% and 40-60% at $\sqrt{s_{NN}} = 3 \text{ GeV}$	34
31	v_2 as a function of rapidity(y) in different centrality bins for π^+ and π^- in Au+Au collisions at $\sqrt{s_{NN}} = 3 \text{ GeV}$	35
32	v_2 as a function of rapidity(y) in different centrality bins for π^+ and π^- in Au+Au collisions at $\sqrt{s_{NN}} = 3 \text{ GeV}$ in 0-10%, 10-40%, 40-60% centrality bins.	36
33	v_2 as a function of p_T in different centrality bins for π^+ and π^- in Au+Au collisions at $\sqrt{s_{NN}} = 3 \text{ GeV}$	36
34	v_2 as a function of p_T in different centrality bins for π^+ and π^- in Au+Au collisions at $\sqrt{s_{NN}} = 3 \text{ GeV}$ in 0-10%, 10-40%, 40-60% centrality bins.	36
35	v_2 as a function of rapidity(y) in different centrality bins for K^+ and K^- in Au+Au collisions at $\sqrt{s_{NN}} = 3 \text{ GeV}$	37
36	v_2 as a function of rapidity(y) in different centrality bins for K^+ and K^- in Au+Au collisions at $\sqrt{s_{NN}} = 3 \text{ GeV}$ in 0-10%, 10-40%, 40-60% centrality bins.	37
37	v_2 as a function of p_T in different centrality bins for K^+ and K^- in Au+Au collisions at $\sqrt{s_{NN}} = 3 \text{ GeV}$	38
38	v_2 as a function of p_T in different centrality bins for K^+ and K^- in Au+Au collisions at $\sqrt{s_{NN}} = 3 \text{ GeV}$ in 0-10%, 10-40%, 40-60% centrality bins.	38
39	proton v_2 as a function of rapidity(y) in different centrality bins in Au+Au collisions at $\sqrt{s_{NN}} = 3 \text{ GeV}$	39
40	proton v_2 as a function of rapidity(y) in different centrality bins for in Au+Au collisions at $\sqrt{s_{NN}} = 3 \text{ GeV}$ in 0-10%, 10-40%, 40-60% centrality bins.	39
41	proton v_2 as a function of p_T in different centrality bins in Au+Au collisions at $\sqrt{s_{NN}} = 3 \text{ GeV}$	40
42	proton v_2 as a function of p_T in different centrality bins in Au+Au collisions at $\sqrt{s_{NN}} = 3 \text{ GeV}$ in 0-10%, 10-40%, 40-60% centrality bins.	40

43	EPD event plane resolution as a function of collision centrality, the black solid circle is first order event plane resolution, black open circle is the converted second order event plane resolution for v_2 calculation, the black solid square is second order event plane resolution.	41
44	TPC and EPD sub-event plane angle (Ψ_2) distribution in different centralities, the black line is raw Ψ_2 distribution, the blue line is Ψ_2 distribution with re-centering calibration, the red line is Ψ_2 distribution with re-centering and shift calibration.	42
45	v_2 as a function of p_T in 3GeV Au+Au collisions, 10-40% centrality from first order and second event plane angle, and their ratio.	43
46	The event plane resolution as a function collision centrality at 3GeV in UrQMD model for first order second order and converted second order.	43
47	v_2 as a function of p_T at 3 GeV 10-40% in UrQMD model from first order and second event plane angle, and their ratio.	44
48	Systematic uncertainty study for v_1 as a function of rapidity in 10-40% for pion at $\sqrt{s_{NN}} = 3$ GeV. Left is v_1 as a function of rapidity from different cut, right is fitted results of dv_1/dy from different source cut	46
49	Systematic uncertainty study for v_2 as a function of rapidity in 10-40% for pion at $\sqrt{s_{NN}} = 3$ GeV.	46
50	Systematic uncertainty study for v_1 as a function of p_T in 10-40% for pion at $\sqrt{s_{NN}} = 3$ GeV	47
51	Systematic uncertainty study for v_2 as a function of p_T in 10-40% for pion at $\sqrt{s_{NN}} = 3$ GeV.	47
52	Systematic uncertainty study for v_1 as a function of rapidity in 10-40% for kaon at $\sqrt{s_{NN}} = 3$ GeV. Left is v_1 as a function of rapidity from different cut, right is fitted results of dv_1/dy from different source cut	48
53	Systematic uncertainty study for v_2 as a function of rapidity in 10-40% for kaon at $\sqrt{s_{NN}} = 3$ GeV.	48
54	Systematic uncertainty study for v_1 as a function of p_T in 10-40% for kaon at $\sqrt{s_{NN}} = 3$ GeV	49
55	Systematic uncertainty study for v_2 as a function of p_T in 10-40% for kaon at $\sqrt{s_{NN}} = 3$ GeV.	49

56	Systematic uncertainty study for v_1 as a function of rapidity in 10-40% for proton at $\sqrt{s_{NN}} = 3$ GeV. Left is v_1 as a function of rapidity from different cut, right is fitted results of dv_1/dy from different source cut	50
57	Systematic uncertainty study for v_2 as a function of rapidity in 10-40% for proton at $\sqrt{s_{NN}} = 3$ GeV.	50
58	Systematic uncertainty study for v_1 as a function of p_T in 10-40% for proton at $\sqrt{s_{NN}} = 3$ GeV	51
59	Systematic uncertainty study for v_2 as a function of p_T in 10-40% for proton at $\sqrt{s_{NN}} = 3$ GeV.	51

LIST OF TABLES

I	Event cuts and total number of minimum bias events	9
II	Bad runs list and what's wrong	10
III	Tracks cuts for TPC event plane reconstruction	12
IV	TPC global tracks cuts for PID	21
V	dE/dX and $mass^2$ cut for PID	21
VI	Systematic cuts for pions and kaons	45
VII	Systematic cuts for proton	45

1 **1. ANALYSIS SETUP**

2 In this section, we mainly discuss the setup of our analysis. We will introduce the conven-
3 tions of fixed target collision mode, and the bad runs selection from run-by-run QA. We will also
4 discuss the data sets and the event and track cut we used in this analysis. Finally, the centrality
5 determination will be discussed.

6 **1.1. Fixed Target Conventions**

7 In the year 2018, STAR collected fixed-target mode data, the center of mass energy $\sqrt{s_{NN}}$ is 3
8 GeV (beam energy of 3.85 GeV/u). There are about 258 M good events, which is enough for our
9 flow analysis. For the fixed target mode collisions, It is not same with collider mode, the lab frame
10 and the center of mass frame are not same, the midrapidity is not 0. For example, we need to boost
11 the measured rapidity in the lab frame by midrapidity into center of mass frame. The midrapidity
12 is half of beam rapidity, beam rapidity can be calculated from this equation.

$$y_b = \cosh^{-1} \left[\frac{\sqrt{s_{NN}}}{2 * m_p} \right] \quad (1)$$

13 Where the $\sqrt{s_{NN}}$ is center of mass energy (3 GeV), the m_p is proton mass (0.938). In our STAR
14 convention, the beam-going direction is the positive direction (the target is located in the negative
15 rapidity direction $y_{target} = -1.045$). In order to match the conventions, when calculating rapidity in
16 center of mass frame, in addition to shift by midrapidity, we also need to flip the sign.

$$y_{CM} = -(y_{lab} - y_{mid}) \quad (2)$$

17 **1.2. Datasets and Event Selection cuts**

18 In the year 2018, STAR has started taken fixed target model collision. In this study, we analyze
19 the minimum bias events for Au + Au collisions at $\sqrt{s_{NN}} = 3$ GeV, single beam energy is 3.85
20 GeV. The trigger information and event selection are summarized in the TABLE I. Since the target
21 is fixed, in our analysis we set the vertex cut along the Z direction is [198, 202] cm, in the X
22 and Y direction, we set the Vr ($\sqrt{Vx^2 + Vy^2}$) less than 2 cm around (0, -2). The total number of
23 minimum bias events is 250 million, and after event cuts (Vz and Vr cut), we still have 220 million
24 good events.

TABLE I. Event cuts and total number of minimum bias events

Energy($\sqrt{s_{NN}}$ GeV)	Trigger ID (minimum bias)	Vz(cm)	Vr((0,-2) cm)	Total Events(M)	Good Events(M)
3.0	620052	[198, 202]	2	258	220

1.3. Badruns selection

Due to the detector performance during the data taking, we need to select the bad runs, which will influence our analysis and results. In our analysis, 7 variables (Vz, Vr, refmult, dca, eta, phi, pt) will be used to select bad runs. With event (Vz and Vr) cut, we plot each variable's mean value as a function of run index in the figure 1, totally there are 191 runs at 3GeV. The First step, in these plots, we give the event cuts (198 < Vz < 202 cm and Vr < 2 cm), and we plot these variable' mean value as a function of run index, the run index is corresponding each run number. The second step, we perform minimum and maximum cut (the blue dash line) for each variable to exclude the extreme data. The third step, we calculate the mean value (red solid line) and 3σ (red dash line) of the rest data. After that, we can select the bad runs, which are outside the 3σ region. totally we have 21 bad runs, these runs will be removed in our analysis.

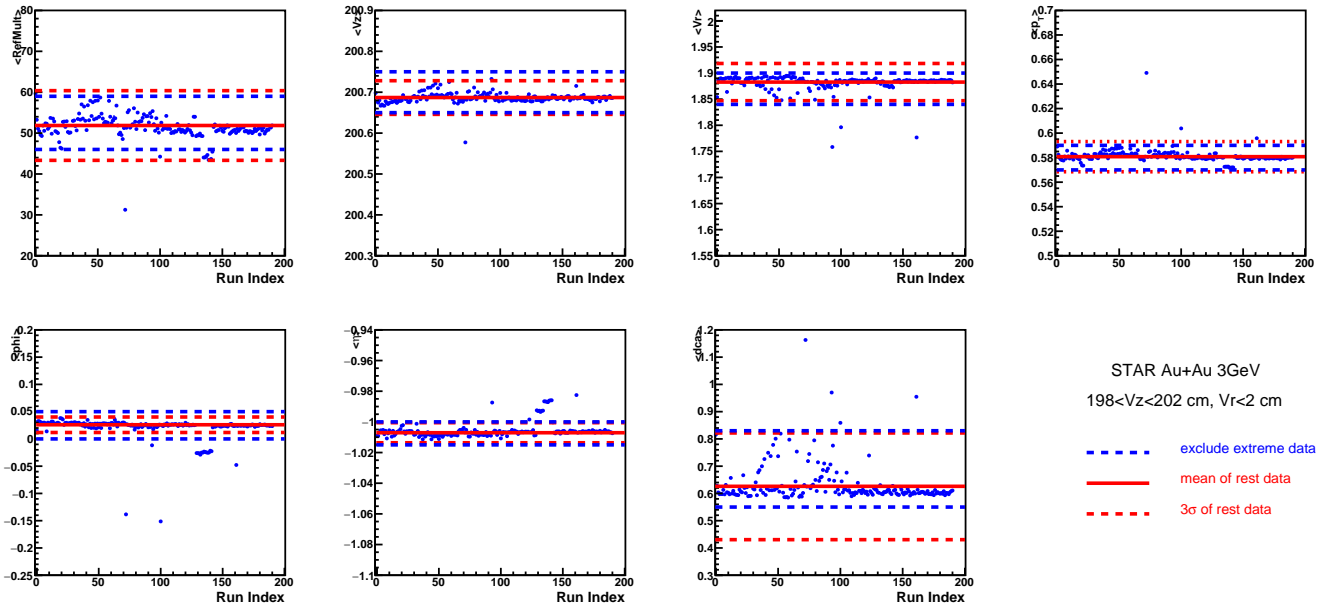


FIG. 1. These variables' (Vz, Vr, refmult, dca, eta, phi, pt) mean value as a function of run index.

Here we list all of the bad runs from this selection and what is wrong with these runs from shift log in the TABLE II This is refer from **Badrungs**

TABLE II. Bad runs list and what's wrong

Bad runs	What's wrong with this run?
19151029	First data run. Fill was with 36 bunches, not 12.
19152001	Run has only 1 event.
19152078	1 minute run, not in the shift log book.
19153023	3.5 minute run, get almost no rate, asked MCR, then TPC trips.
19153032	35 second run, run stopped with TPC trips.
19153065	35 second run, run stopped with two inner TPC trips.
19154012-19154024	TPC sector 14 has four RDOs missing.
19154026	BTOW is out for this run.
19154051	45 second run, inner TPC tripped during the run.

³⁸ **1.4. Centrality Determination**

³⁹ Since the centrality definition is studied by Sorooaj, I will discuss with him and update this
⁴⁰ section later.

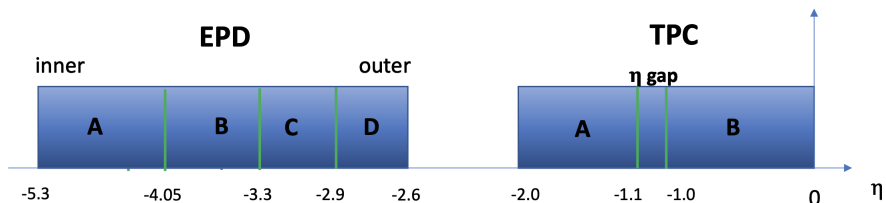
41 **2. ANALYSIS DETAIL**

42 In this section, we will discuss the analysis detail, since in this analysis, the event plane method
43 is used to calculate the directed flow (v_1) and elliptic flow (v_2). By following the standard event
44 plane method, firstly we discuss the event plane reconstruction from TPC(Time Projection Cham-
45 ber) and EPD(Event Plane Detector), TPC's η coverage is $[-1, 1]$, and the EPD is located at the
46 forward rapidity region, $\eta \in (-5.1, -2.1)$. Since it is Fix target model collision in this analysis, the
47 acceptance of final state particle is not symmetric around mid-rapidity, we cannot use 2-sub event
48 method to calculate the resolution, which is used in the BES-I collider model collision, the 2-sub
49 event method requires each sub-event has similar multiplicity and resolution. So, in this analy-
50 sis, we employ 3-sub event method to calculate the resolution. After that, we will do the particle
51 identification (PID) for pion, kaon proton, then, we introduce the v_1 and v_2 calculation.

52 **2.1. Event Plane Reconstruction**

53 We will separately introduce the first-order and second-order Event Plane Reconstruction from
54 TPC and EPD.

55 In order to calculate the resolution for each event plane, we divide the TPC to 2-sub events
56 and EPD to 4-sub events based on their pseudorapidity (η) range. In the figure 2, we show the
57 schematic plot of TPC and EPD sub-events. Since it's fixed-target model collision, we only mea-
58 sure the negative pseudorapidity (η) region. In the collider model, the origin point of the Lab frame
59 is in the center of TPC , the EPD is located at $\eta \in (-5.1, 2.1)$. In the fixed-target model, the origin
60 point of the Lab frame is shifted to the edge of TPC, as a result that the η of EPD is boosted at $\eta \in$
61 $(2.6, 5.3)$.



62 FIG. 2. The schematic plot of TPC and EPD sub-events

64 **2.1.1. TPC Event Plane Reconstruction**

65 The event plane method correlates each particle with the event plane determined from these
 66 particles without the particle of interest, which can be done for each harmonic. Here we only
 67 discuss the first-order event plane reconstruction. For TPC event plane, these tracks, that are
 68 required to pass the following cuts in the table III, will be used: In order to calculate the first-order

TABLE III. Tracks cuts for TPC event plane reconstruction

-2.0 < η < -1.1 (for TPC-A)
-1.0 < η < 0 (for TPC-B)
nHitsFit > 15
nHitsFit/nHitsMax > 0.52
dca < 3 (cm)
0.2 < p_T < 2.0 (GeV/c)

69

70

71 event plane angle, firstly we construct the Q vector from particle's azimuthal angle. And the event
 72 plane angle can be calculated based on the Q vector.

$$\vec{Q} = \begin{pmatrix} Q_y \\ Q_x \end{pmatrix} = \begin{pmatrix} \sum_i w_i \sin(\phi) \\ \sum_i w_i \cos(\phi) \end{pmatrix} \quad (3)$$

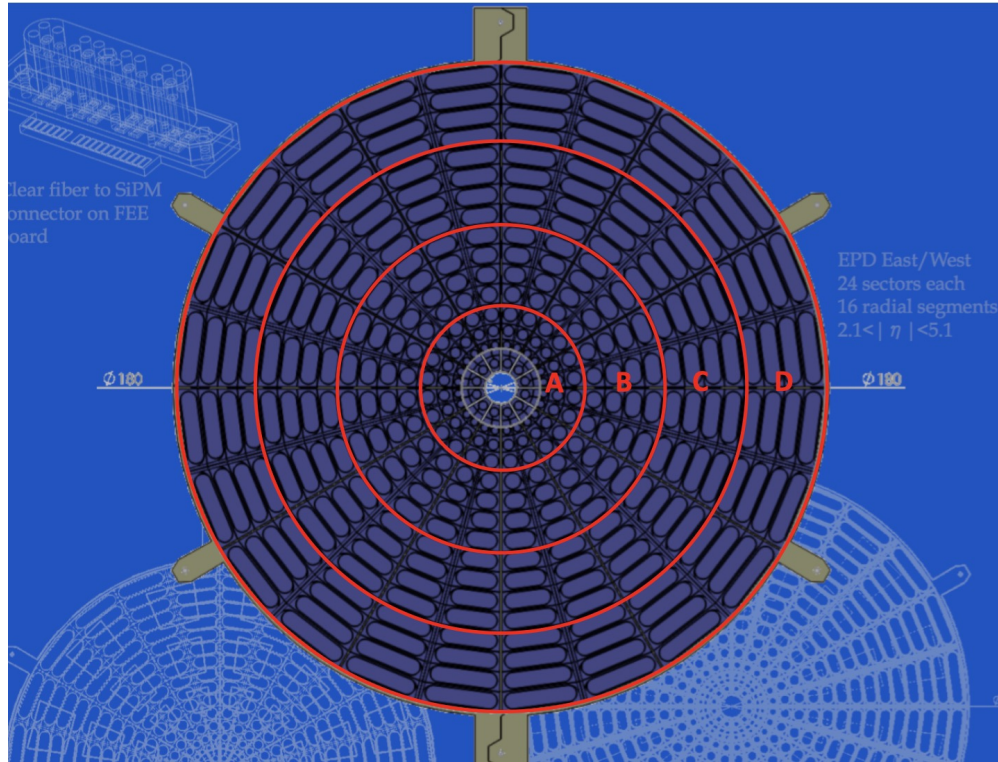
$$\Psi_1 = \tan^{-1} \left(\frac{\sum_i w_i \sin(\phi)}{\sum_i w_i \cos(\phi)} \right) \quad (4)$$

$$w_i = \begin{cases} p_T, 0.2 < p_T < 2.0 (\text{GeV}/c) \\ 2.0, p_T > 2.0 (\text{GeV}/c) \end{cases} \quad (5)$$

73 Where sums extend over all particles i used in the event plane calculation, and ϕ is particle
 74 azimuthal angle in the laboratory frame, and w_i is the weight for the i^{th} particle, here we use the
 75 p_T as the weight. The Ψ_1 is the first-order event plane angle. The reaction plane azimuthal angle
 76 distribution should be isotropic in the laboratory frame if the detectors have ideal acceptance. But
 77 the detectors always have non-uniform acceptance. In order to remove the acceptance correlations
 78 from the imperfect detector, we must make the event plane angle distribution isotropic or flat. A
 79 procedure for flattening the laboratory event plane angle distribution is necessary. In this analysis,
 80 we perform the re-centering and shift calibration to make the event plane angle distribution flat.

81 2.1.2. EPD Event Plane Reconstruction

82 The event plane reconstruction using EPD is similar to TPC. While the TPC measures the tracks
 83 and EPD measures the ADC (analog-digital converter) value in each sectors. In the figure 3, we
 84 show the schematic plot of EPD (Event Plane Detector). As we can see, EPD has 16 rings, there
 85 are 24 sectors in the ring, while there are 12 sectors in the inner most ring, totally the EPD has 372
 86 sectors, we can measure the azimuthal angle for each sector. As we can see, in the figure 3, we
 87 divide the EPD to 4 groups based on the rings. From inner to outer, EPD-A (1-4 ring), EPD-B (5-8
 88 ring), EPD-C (9-12 ring), EPD-D (13-16 ring). We will reconstruct the event plane in these EPD
 89 groups separately. For the event plane reconstruction, we also construct the Q vector and calculate



90 FIG. 3. The schematic plot of EPD and EPD sub-events
 91

92 the event plane angle based on the Q vector.

$$\vec{Q} = \begin{pmatrix} Q_y \\ Q_x \end{pmatrix} = \begin{pmatrix} \sum_i w_i \sin(\phi) \\ \sum_i w_i \cos(\phi) \end{pmatrix} \quad (6)$$

$$\Psi_1 = \tan^{-1} \left(\frac{\sum_i w_i \sin(\phi)}{\sum_i w_i \cos(\phi)} \right) \quad (7)$$

$$w_i = \begin{cases} nMip, 0.3 < nMip < 2.0 \\ 2.0, nMip > 2.0 \end{cases} \quad (8)$$

Where sums goes over all hits detected by EPD, and ϕ is azimuthal angle of EPD sectors in the laboratory frame, and w_i is the weight for the i^{th} hits, here we use the nMip as the weight, which is the calibrated ADC value. The Ψ_1 is the first-order event plane angle. As we discussed before, we will also consider the acceptance correlations from the imperfect detector and perform re-centering and shift calibration to make the event plane angle distribution flat. In the figure 4, we show the EPD azimuthal angle ϕ and pseudorapidity η distribution using two styles, which means 1: the ϕ and η in the center position of the corresponding tile. 2: the ϕ and η value in the random position of the corresponding tile. Although the two styles have different distribution, the results of resolution and v_1, v_2 value using two styles are same.

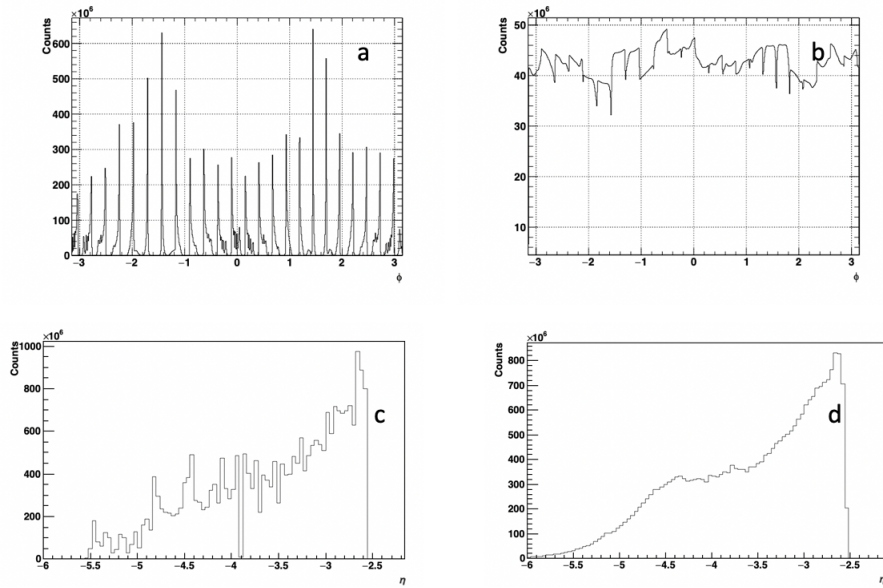


FIG. 4.

2.1.3. re-centering and shift calibration

The re-centering is a track-by-track calibration. One subtracts the factor from the Q-vector of each event, in which the factor is the Q-vector averaged over many events. After that, we can calculate the event plane angle. As we can see in the following equation. It is not enough that we

106 only do the re-centering calibration. We will do the shift calibration further. The shift calibration
 107 is that one fits the non-flat distribution of Ψ_n averaged over many events with a Fourier expansion
 108 and calculates the shifts for each event Ψ_n necessary to force a flat distribution on average. The
 109 re-centering and shift calibration are all run-by-run and centrality-by-centrality calibration.

$$\vec{Q}_{rc} = \begin{pmatrix} Q_{y,rc} \\ Q_{x,rc} \end{pmatrix} = \sum_i^N \begin{pmatrix} w_i \sin(\phi_i) - \langle w_i \sin(\phi_i) \rangle \\ w_i \cos(\phi_i) - \langle w_i \cos(\phi_i) \rangle \end{pmatrix} \quad (9)$$

$$\Psi_{1,rc} = \tan^{-1} \frac{Q_{y,rc}}{Q_{x,rc}} \quad (10)$$

$$\Psi_{1,shift} = \sum_i^N \frac{2}{i} [-\langle \sin(i\Psi_{1,rc}) \rangle \cos(i\Psi_{1,rc}) + \langle \cos(i\Psi_{1,rc}) \rangle \sin(i\Psi_{1,rc})] \quad (11)$$

$$\Psi_1 = \Psi_{1,rc} + \Psi_{1,shift} \quad (12)$$

110 Where the \vec{Q}_{rc} is the Q-vector after re-centering calibration, the $\Psi_{1,rc}$ is the first-order event
 111 plane angle after re-centering calibration. Then we substitute the $\Psi_{1,rc}$ into that equation to get the
 112 shift factor, the N goes 20th order. Thus we get the flat first-order event plane angle Ψ_1 . Then we
 113 have the first-order event plane angle distribution in the figure 5, as we can see from bottom to top
 114 (TPC-A, TPC-B, EPD-A, EPD-B, EPD-C, EPD-D), from right to left (0-5% ... 70-80%), the black
 115 line is raw Ψ_1 distribution without any flat calibration, the blue line is the Ψ_1 distribution with re-
 116 centering calibration, it's more flat than black, the red line is Ψ_1 distribution with re-centering
 117 and shift calibration, after that, we have the isotropic or flat Ψ_1 , which can correct the detector
 118 acceptance effect and be used to calculate the v_1 and v_2 . We also look the correlation between
 119 different sub-events in the figure 6, because we measure the same event plane in the different η
 120 range, after fattening event plane distribution, they should have strong correlation.

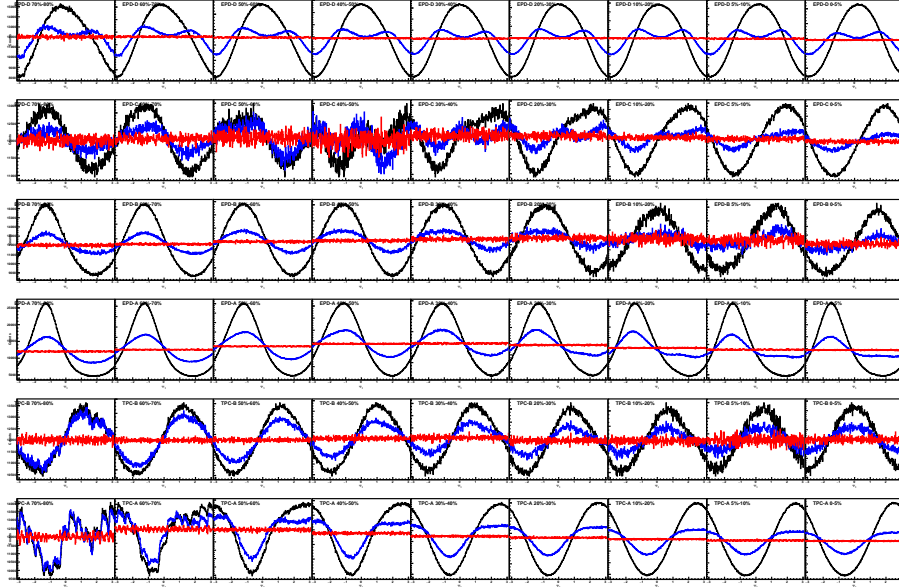


FIG. 5. TPC and EPD sub-event Ψ_1 distribution in different centrality, the black line is without raw Ψ_1 distribution, the blue line is with re-centering calibration, the red line is with re-centering and shift calibration

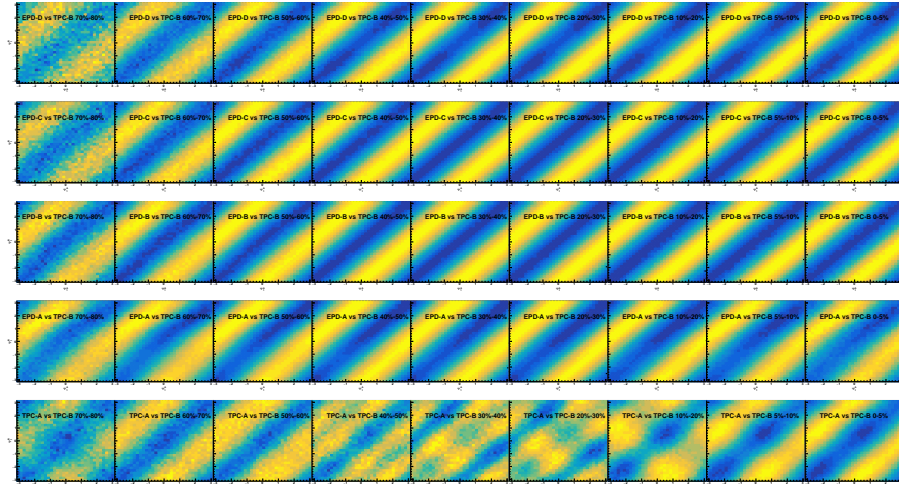


FIG. 6. TPC and EPD sub-event event plane angle (Ψ_1) correlation

122 2.2. Event Plane Resolution

123 Since the azimuthal angle of reaction plane is unknown, we use the event plane angle to estimate
 124 the reaction plane angle. Once we have the event plane angle (Ψ_1), then we can calculate the
 125 observed azimuthal anisotropy parameter (v_1, v_2). But the event plane deviates from the reaction

126 plane, we need to correct the observed azimuthal anisotropy parameter (v_1 , v_2) by event plane
 127 resolution.

$$v_n = \frac{v_n^{obs}}{R_n} = \frac{v_n^{obs}}{\langle \cos[km(\Psi_m - \Psi_r)] \rangle} \quad (13)$$

128 Where the R_n is resolution, v_n is the n^{th} harmonic azimuthal anisotropy parameter, and Ψ_m is the
 129 m^{th} harmonic order event plane, k is integer number $n = k*m$, Ψ_r is reaction plane angle. The
 130 angle brackets denotes an average over all particles in all events. The event plane resolution can
 131 be expressed as:

$$\langle \cos[km(\Psi_m - \Psi_r)] \rangle = \frac{\sqrt{\pi}}{2\sqrt{2}} \chi_m \exp(-\chi_m^2/4) \times [I_{(k-1)/2}(\chi_m^2/4) + I_{(k+1)/2}(\chi_m^2/4)] \quad (14)$$

132 Where $\chi_m \equiv v_m/\sigma$ and I_ν is the modified Bessel function of the order ν . The resolution function
 133 is plotted in the figure 7, the resolution is decreasing with k increases. Note that, numerically,
 134 when $m = 1$, the first order event plane angle can be used to calculate all v_n term. In this analysis,
 135 we will use the first order event plane angle (Ψ_1) to calculate v_1 and v_2 . Another reason is that,
 136 the magnitude of n^{th} harmonic resolution is proportional to multiplicity and flow signal, the v_2 is
 137 decreasing with energy decreases. The second order event plane resolution is quite small at 3 GeV,
 138 which will induce large error for the v_2 results. While the v_1 is increasing with energy decreases.
 139 The error of v_2 calculated from Ψ_1 is 5 times smaller than that from Ψ_2 . It will be discussed in the
 140 result part.

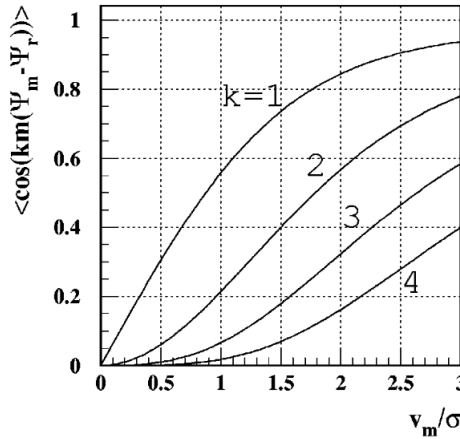


FIG. 7. The event plane resolution for the n^{th} ($n=km$) harmonic of the particle distribution with respect to the m^{th} harmonic plane, as a function of v_m/σ .

141 Since we will use Ψ_1 to calculate v_1 and v_2 , then we substitute ($m=1$, $k=1$) and ($m=1$, $k=2$) into

¹⁴² the resolution equation to calculate the resolution for v_1 and v_2 . v_1 and v_2 can be calculated with
¹⁴³ resolution shown in the following.

$$R_1 = \langle \cos(\Psi_1 - \Psi_r) \rangle = \frac{\sqrt{\pi}}{2\sqrt{2}} \chi_1 \exp(-\chi_1^2/4) \times [I_0(\chi_1^2/4) + I_1(\chi_1^2/4)] \quad (15)$$

¹⁴⁴

$$R_{12} = \langle \cos(2(\Psi_1 - \Psi_r)) \rangle = \frac{\sqrt{\pi}}{2\sqrt{2}} \chi_1 \exp(-\chi_1^2/4) \times [I_{1/2}(\chi_1^2/4) + I_{3/2}(\chi_1^2/4)] \quad (16)$$

¹⁴⁵

$$v_1 = \frac{v_1^{obs}}{R_1} = \frac{\langle \cos(\phi - \Psi_1) \rangle}{\langle \cos(\Psi_1 - \Psi_r) \rangle} \quad (17)$$

¹⁴⁶

$$v_2 = \frac{v_2^{obs}}{R_{12}} = \frac{\langle \cos(2(\phi - \Psi_1)) \rangle}{\langle \cos(2(\Psi_1 - \Psi_r)) \rangle} \quad (18)$$

¹⁴⁶ Where the R_1 is the first order event plane resolution for v_1 and R_{12} is converted resolution for v_2
¹⁴⁷ calculation. In the equation 15, the χ_1 is unknown. But we can first using three sub-event method
¹⁴⁸ to calculate the left hand first order event plane resolution (R_1), then we can determine the χ_1 , thus
¹⁴⁹ we substitute χ_1 into equation 16 to get the converted resolution for v_2 calculation (R_{12}).

¹⁵⁰ In the previous BES-I collider mode analysis, the resolution is determined from two sub-event
¹⁵¹ method, which is required the multiplicity and flow signal of sub-events are same. This can be
¹⁵² done by dividing the two sub-event from negative and positive η range. But, if the sub-events
¹⁵³ are not "equal", or if we have only correlations between particles in different windows, and the
¹⁵⁴ resolution in each window can be different, then one needs at least three sub-events to determine
¹⁵⁵ the event plane resolution in each of them. In this case, the resolution in the first window is
¹⁵⁶ determined as:

$$\langle \cos(\Psi_1^a - \Psi_r) \rangle = \sqrt{\frac{\langle \cos(\Psi_1^a - \Psi_1^b) \rangle \langle \cos(\Psi_1^a - \Psi_1^c) \rangle}{\langle \cos(\Psi_1^b - \Psi_1^c) \rangle}} \quad (19)$$

¹⁵⁷ It's similar way to determine the other sub-event resolution. In this analysis, we divide the EPD
¹⁵⁸ to 4 sub-event groups, and we also combine the first two and last two group into one group,
¹⁵⁹ thus we have 6 sub-event groups and their resolution. as you can see in the figure 8, the first
¹⁶⁰ order event plane resolution as a function of centrality, different color and symbol means the same
¹⁶¹ interest event plane resolution using different reference event plane. From EPD-A to EPD-D, the
¹⁶² resolution is decreasing with pseudorapidity decreases. This can be explained from that the v_1
¹⁶³ signal is decreasing with pseudorapidity decreases.

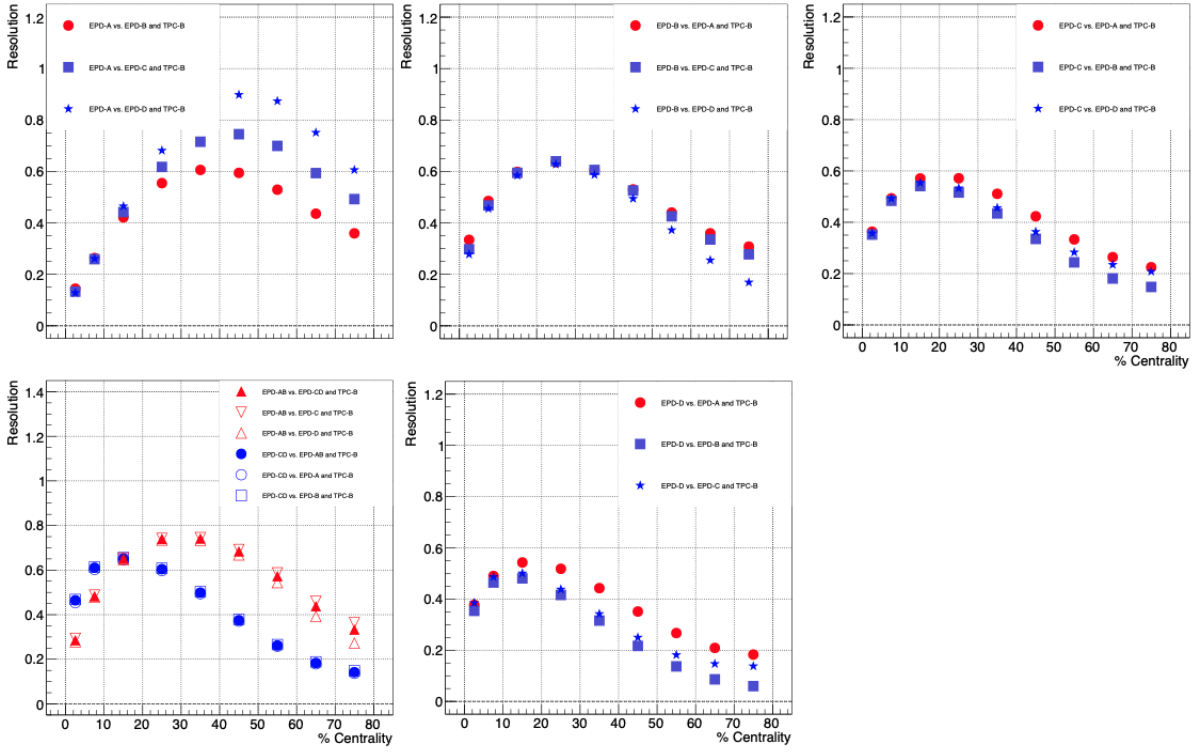


FIG. 8. EPD First order event plane resolution as a function of centrality for different sub-event groups. Different symbol means the same interest event plane resolution using different reference event plane.

164

2.3. Particle Identification

165

2.3.1. PID from TPC and TOF

166

In this analysis, we use TPC and TOF detectors to identify particles (pion, kaon, and proton).

167

Figure 9, the left side, shows the TPC energy loss dE/dx as a function of rigidity (p/q) with quality cuts. The curves for different color indicate the Bichsel expectation values for corresponding particles. As we can see, the TPC can identify particles at low momentum as illustrated by the color bands. At high momentum region, we need to identify particles together with TOF information. Figure 9, the right side, shows the measured mass square as a function of rigidity (p/q) with track quality cuts.

173

The $\langle dE/dx \rangle$ distribution for a fixed particle type is not Gaussian.ref”M. Aguilar-Benitez et al.,

174

Z. Phys. C 50, 405 (1991).” It has been shown that a better Gaussian variable, for a given particle

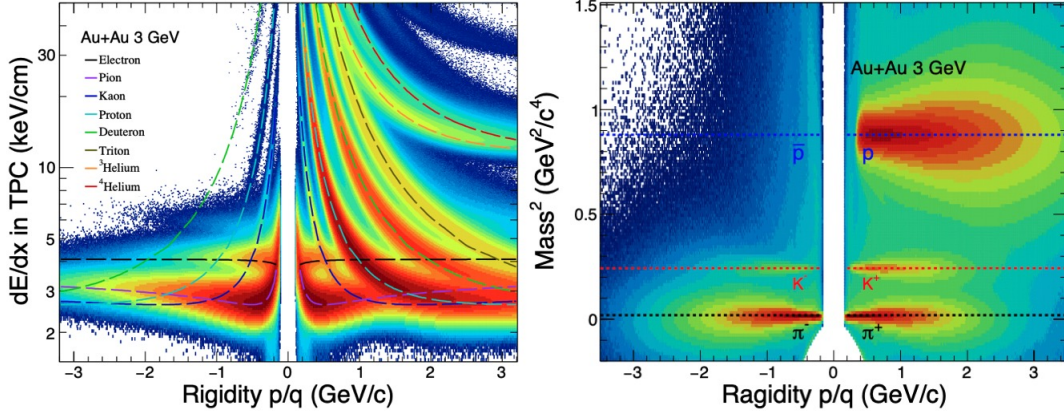


FIG. 9. Left: Energy loss dE/dx as a function of rigidity (p/q) for Au+Au collisions at $\sqrt{s_{NN}} = 3$ GeV. The dash lines indicate the theoretical predicated values for different particles. Right: $Mass^2$ as a function of rigidity (p/q) for Au+Au collisions at $\sqrt{s_{NN}} = 3$ GeV. The dash lines indicate the corresponding particles.

¹⁷⁵ type, is the $n\sigma_{particles}$, defined as:

$$n\sigma_{particle} \propto \ln \left[\left\langle \frac{dE}{dX} \right\rangle_{particle} / \left\langle \frac{dE}{dX} \right\rangle_{Bichsel} \right] \quad (20)$$

¹⁷⁶ where the particle type ($e^\pm, \pi^\pm, K^\pm, p, or \bar{p}$) and $\left\langle \frac{dE}{dX} \right\rangle_{Bichsel}$ is the corresponding Bichsel function.

¹⁷⁷ The most probable value of Bichsel function for the particle is 0.

¹⁷⁸ The variable mass square (m^2) from TOF is given by:

$$m^2 = p^2 \left(\frac{c^2 T^2}{L^2} - 1 \right) \quad (21)$$

¹⁷⁹ where the p is the momentum, T is the time of travel by particle, L is the path length, and c is the
¹⁸⁰ speed of light.

¹⁸¹ 2.3.2. Acceptance of pion, kaon and proton

¹⁸² In order to avoid fake tracks in the TPC and to improve the average momentum and energy loss

¹⁸³ resolution, the following track quality cuts in the table IV were applied, then for the identification
¹⁸⁴ of pion, kaon and proton, we require TPC $n\sigma$ and TOF $mass^2$ cuts in the table V. After these
¹⁸⁵ cuts, we have these particles' acceptance plot (π^\pm, K^\pm, p) in the figure V, we also label the target
¹⁸⁶ location at $y = -1.045$.

TABLE IV. TPC global tracks cuts for PID

nHitsFit>15
nHitsFit/nHitsMax>0.52
dca < 3 (cm)

 TABLE V. dE/dX and $mass^2$ cut for PID

particle	cuts
pion	$ n\sigma_\pi < 3$ and $-0.1 < mass^2 < 0.15$
kaon	$ n\sigma_{kaon} < 3$ and $0.16 < mass^2 < 0.36$
proton	$ n\sigma_{proton} < 2$

187 2.3.3. *Purity*

188 **2.4. Efficiency Correction**

189 **2.4.1. TPC tracking efficiency**

190 The detector acceptance and the efficiency of reconstructing particle tracks are determined to-
 191 gether by embedding Monte Carlo tracks simulated using the GEANT model of the STAR detector
 192 into real events at the raw data level. One important requirement is to have a match in the distribu-
 193 tions of reconstructed embedded tracks and real data tracks for quantities reflecting track quality
 194 and used for track selection. The ratio of the distribution of reconstructed and original Monte
 195 Carlo tracks as a function of p_T and rapidity gives the efficiency x Acceptance correction factor
 196 for the p_T and rapidity interval studies. Figure 11, 12, 13, 14 shows the pion, kaon and proton TPC
 197 tracking efficiency as a function of p_T and rapidity. The track-by-track TPC tracking efficiency
 198 correction will be included in this analysis.

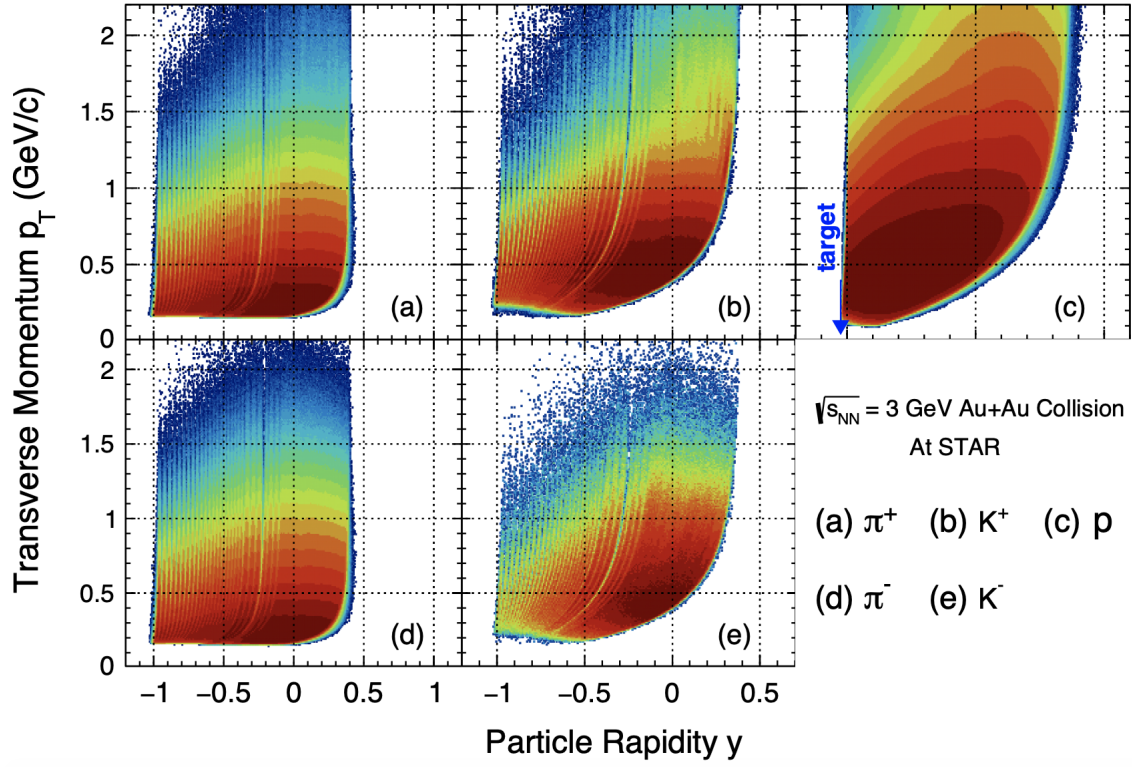


FIG. 10. Rapidity(y) and transverse momentum(p_T) acceptance of $\pi^\pm, K^\pm, proton$ using TPC and TOF in Au+Au collisions at $\sqrt{s_{NN}} = 3$ GeV. The target is located at the $y = -1.045$.

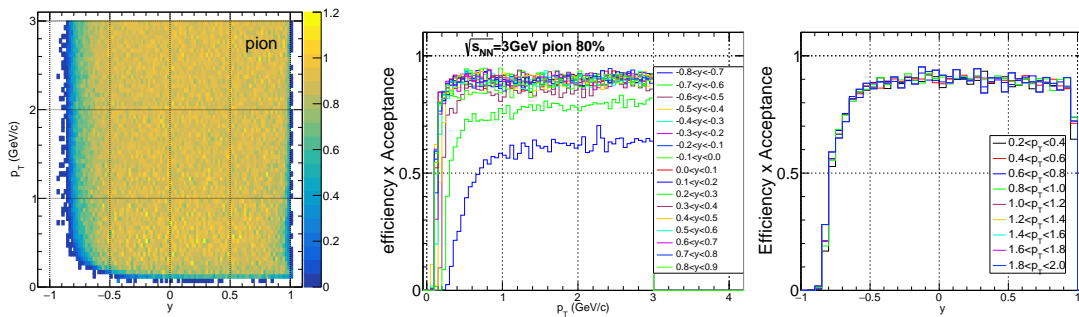


FIG. 11. pion TPC tracking efficiency as a function of p_T and rapidity for two-dimensional and separately.

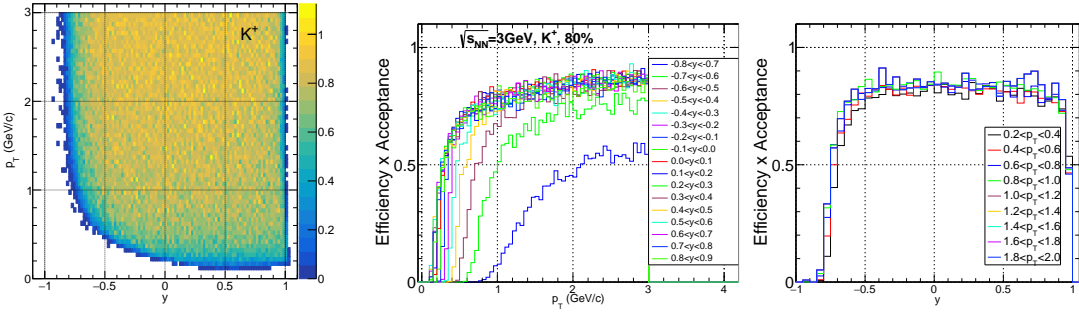


FIG. 12. K^+ TPC tracking efficiency as a function of p_T and rapidity for two-dimensional and separately.

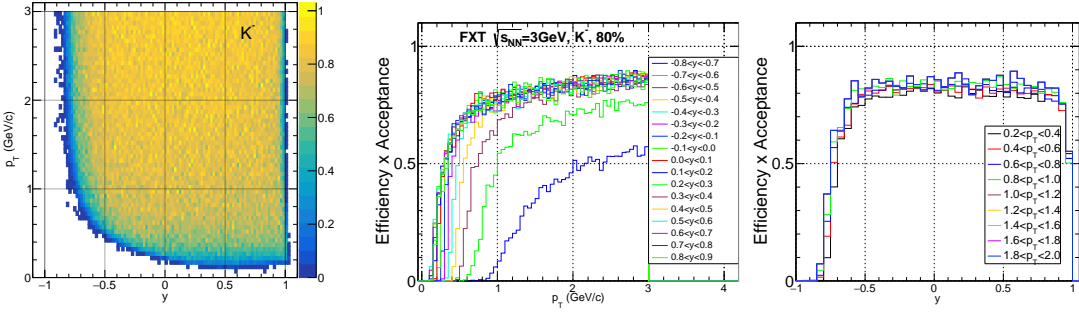


FIG. 13. K^- TPC tracking efficiency as a function of p_T and rapidity for two-dimensional and separately.

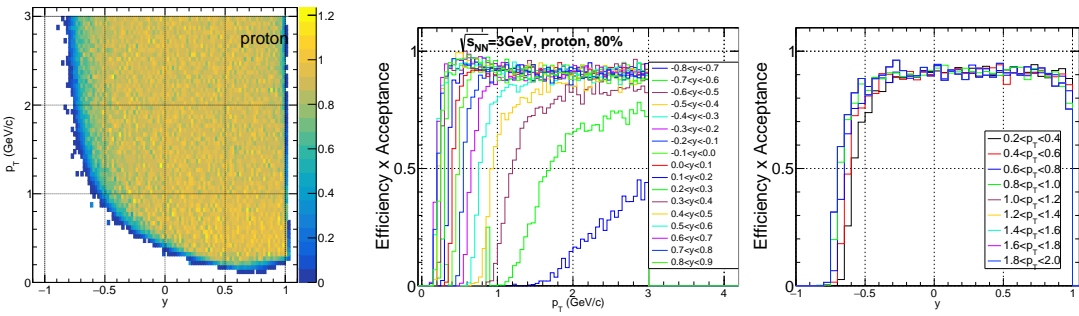


FIG. 14. proton TPC tracking efficiency as a function of p_T and rapidity for two-dimensional and separately.

199 **3. RESULTS**

200 In this section, we will introduce the results of v_1 and v_2 for pions, kaons, and proton. We will
201 show their p_T and rapidity and centrality dependence then make discussion with these results. We
202 will also show these results in 0-10%, 10-40%, and 40-60% centrality bins, and make comparison
203 to our STAR published data.

204 **3.1. v_1 results for π, K, p**

205 In this sub-section, we will show the v_1 as a function of p_T and rapidity(y) in fine centrality
206 bins for π^\pm, K^\pm and proton. In the v_1 vs. rapidity distribution, in order to quantify the strength of
207 v_1 , we will fit the v_1 vs. y distribution with this equation 24. As can see, pion's v_1 is positive in the
208 central collision while is negative in the mid-central and peripheral collision.

$$v_1(y) = F * y + C * y^3 + b \quad (22)$$

209 Where parameter F is the v_1 slop dv_1/dy , parameter C is the fluctuation term and parameter b is
210 the offset to origin point.

211 **3.1.1. pions v_1 as a function of p_T and rapidity**

212 Figure 15 shows $\pi^+, \pi^- v_1$ as a function of y for different centrality bins from 0-5% to 50-60%,
213 the red line is fitting function 24, the p_T range is [0.2, 1.6] GeV/c, which is same with STAR BES-I
214 results. We also write down the fitted results v_1 slope dv_1/dy . As we can see, the magnitude of
215 pions' v_1 has centrality dependence, figure 16 shows $\pi^+, \pi^- dv_1/dy$ as a function of centrality, we
216 can clear see that the v_1 sign change from central to peripheral collision. This can be explained
217 by the shadowing effect from spectators, because at 3 GeV, the passage time is comparable or
218 larger than medium expansion time. So, the spectators will shadow the expansion of mediums,
219 which will cause negative v_1 value, and this effect larger with collisions from central collision to
220 peripheral collision.

221 Since STAR's BES-I directed flow results focus on the intermediate centrality interval 10-40%.
222 In this analysis, we also have v_1 results in such centrality bins for these particle species, and,
223 we will calculate the energy dependence for all particles' v_1 . Figure 17 shows π^+ and $\pi^- v_1$ as

²²⁴ a function of y in 0-10%, 10-40% and 40-60% bins. We can see in the 0-10%, the pions' v_1 is
²²⁵ positive, and the the pions' v_1 is negative in the 10-40% and 40-60% centralities, which can be
²²⁶ explained by the spectator shadowing effect.

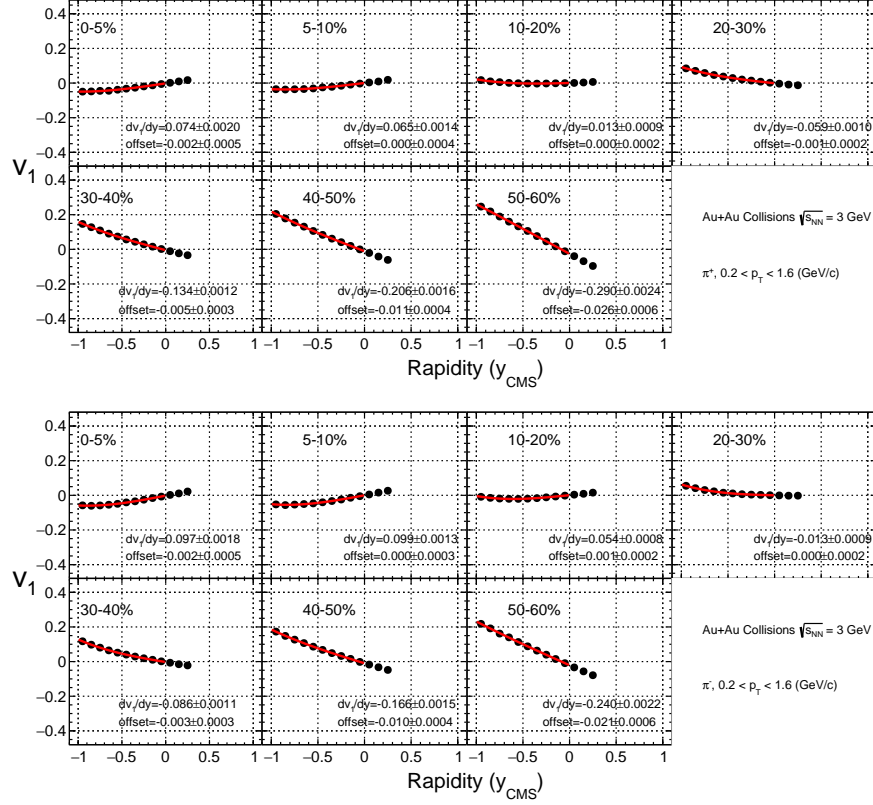


FIG. 15. v_1 as a function of rapidity(y) in different centrality bins for π^+ and π^- in Au+Au collisions at $\sqrt{s_{NN}}$. The red line is fitting function.

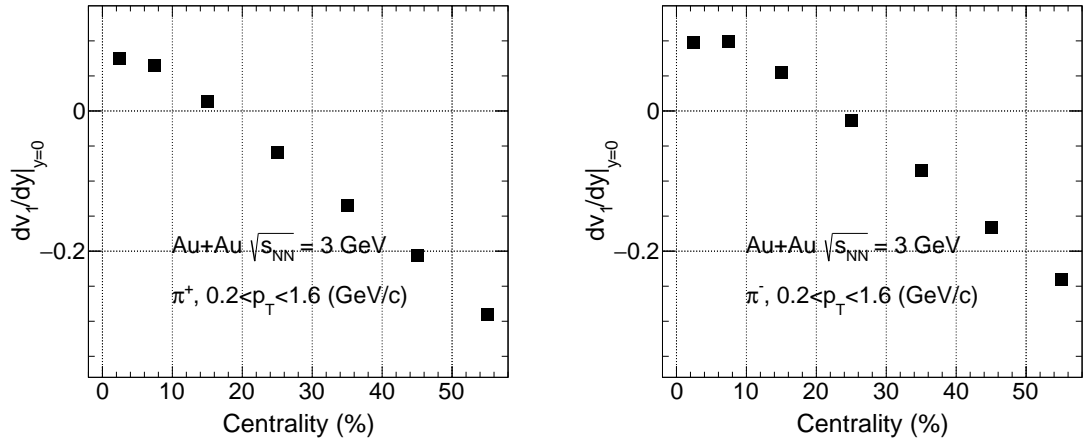


FIG. 16. pions' v_1 slope dv_1/dy as a function of centrality, (left) π^+ (right) π^- in Au+Au collisions $\sqrt{s_{NN}} = 3 \text{ GeV}$.

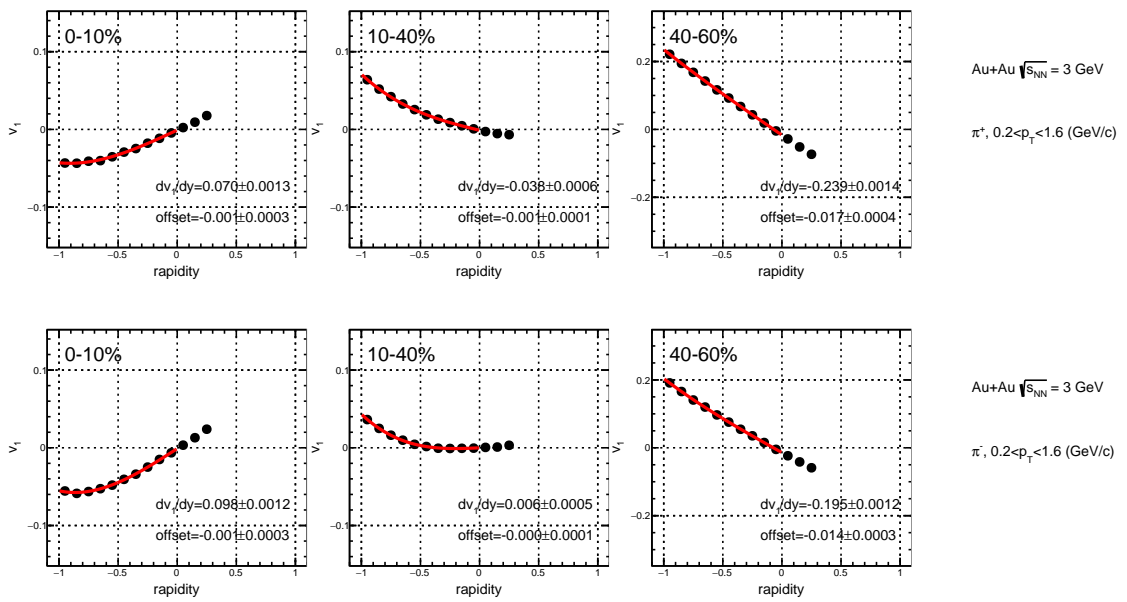


FIG. 17. pions' v_1 as a function of rapidity(y) in Au+Au collision at $\sqrt{s_{NN}} = 3 \text{ GeV}$ in 0-10%, 10-40% and 40-60% bins.

227 Figure 18 shows π^+ and π^- v_1 as a function of p_T in different centrality bins. As we can see,
 228 pions v_1 is increasing with p_T increasing. Figure 19 also shows the results in the wider centrality
 229 bins.

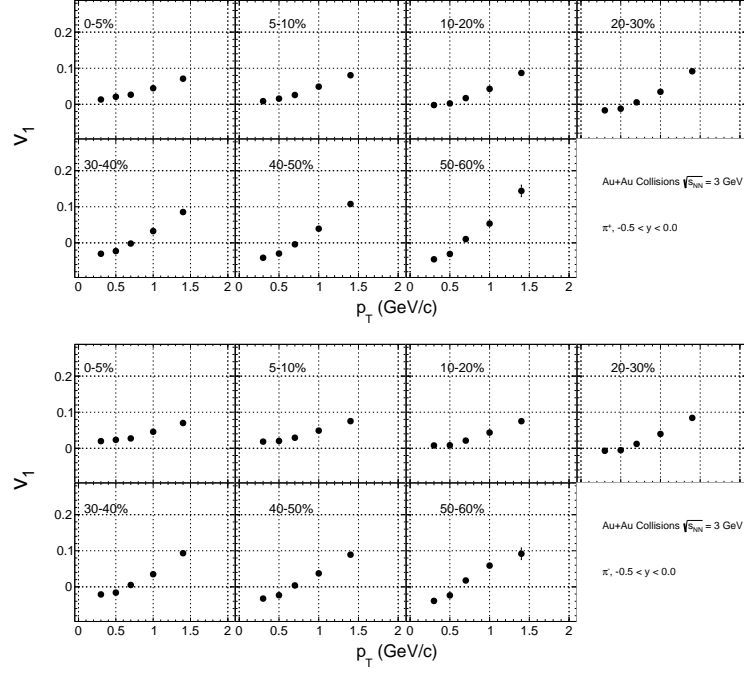


FIG. 18. pions' v_1 as a function of transverse momentum (p_T) in Au+Au collisions at $\sqrt{s_{NN}} = 3$ GeV.

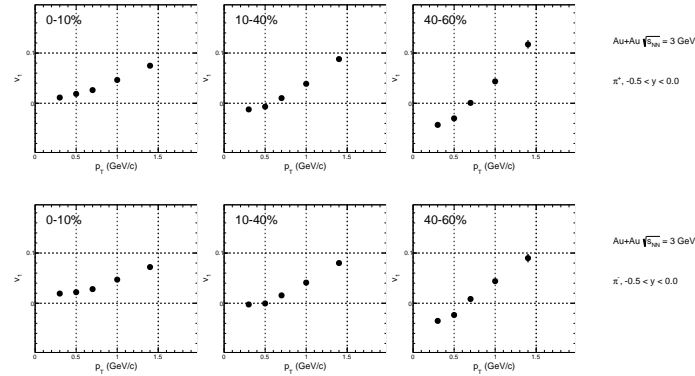


FIG. 19. pions' v_1 as a function of transverse momentum (p_T) in Au+Au collisions at $\sqrt{s_{NN}} = 3$ GeV in 0-10%, 10-40% and 40-60% centrality bins.

230 *3.1.2. kaons' v_1 as a function of p_T and rapidity*

231 Figure 20 shows $K^+, K^- v_1$ as a function of y for different centrality bins from 0-5% to 50-60%,
 232 The red line is fitting function 24, p_T range is [0.4, 1.6] GeV/c, which is same with STAR BES-I
 233 results. As we can see, the magnitude of kaons' v_1 has weak centrality dependence, which is not
 234 same with pions' case, this might be due to kaon has smaller hadronic scattering cross section than
 235 pions, and the v_1 between K^+ and K^- is very similar, figure 26 shows $K^+, K^- dv_1/dy$ as a function
 236 of centrality. In order to make comparison to STAR BES-I results, we have these results in wider
 237 centrality bin in the figure 22. And their v_1 slope is decreasing from central collision to peripheral
 238 collision.

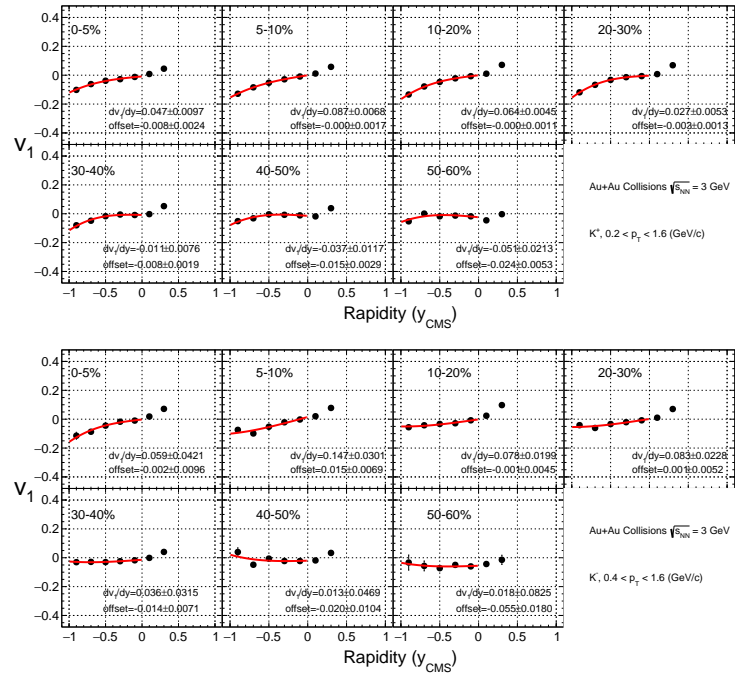
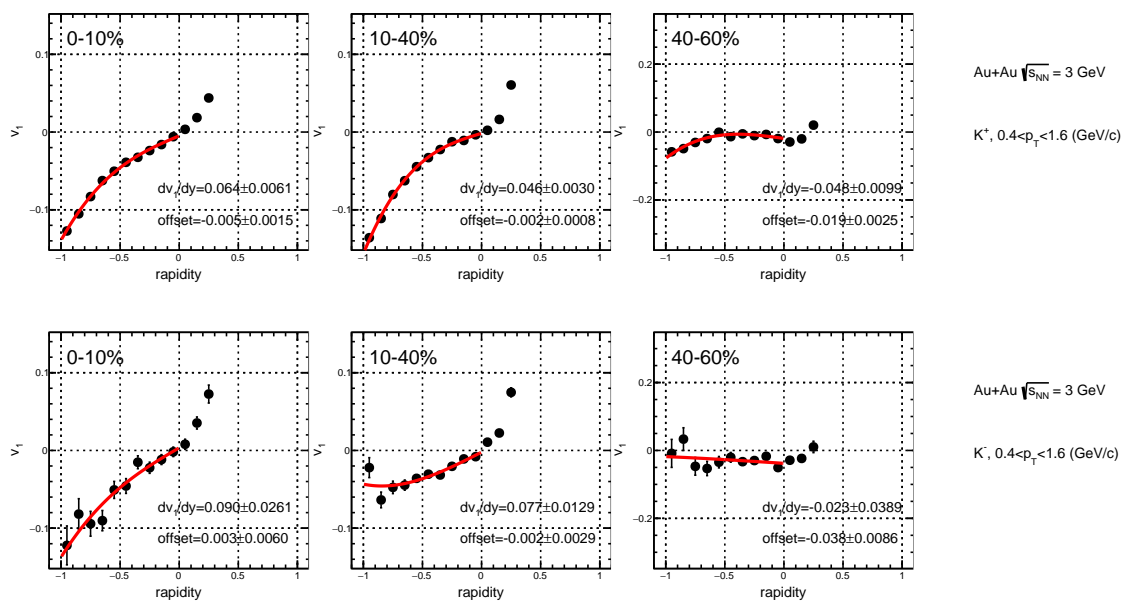
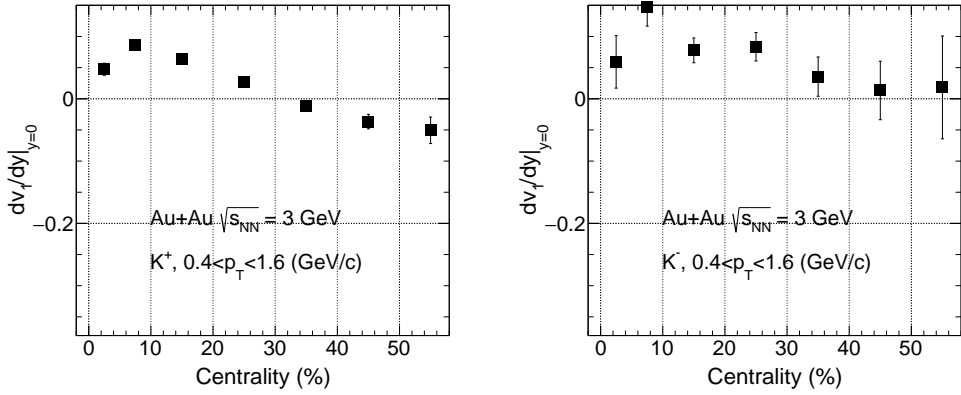


FIG. 20. v_1 as a function of rapidity(y) in different centrality bins for K^+ and K^- in Au+Au collisions at $\sqrt{s_{NN}}$. The red line is fitting function.



239 We also study the p_T dependence of kaons' v_1 in the mid-rapidity region ($-0.5 < y < 0$) in different
 240 centrality bins in the figure 23. As we can see, kaons v_1 is increasing with p_T increasing. Figure 24
 241 also shows the results in the wider centrality bins.

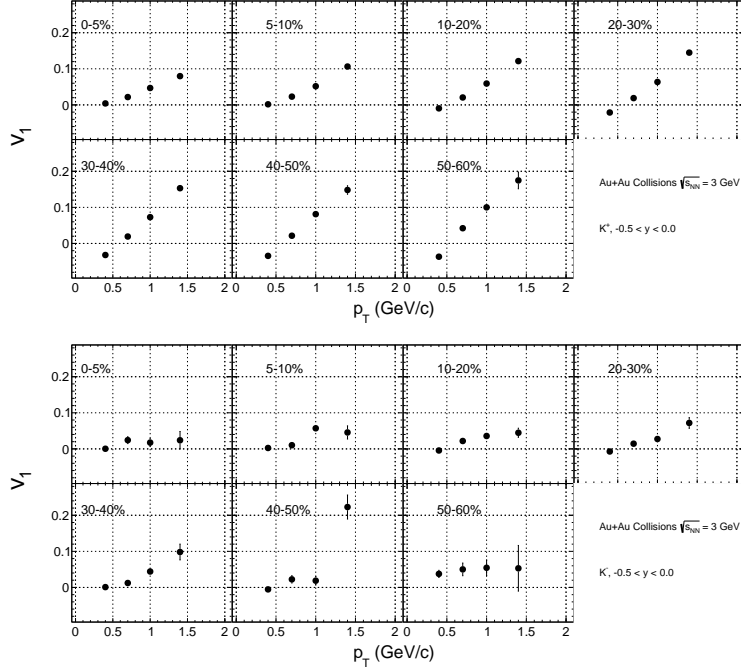


FIG. 23. kaons' v_1 as a function of transverse momentum (p_T) in Au+Au collisions at $\sqrt{s_{NN}} = 3$ GeV.

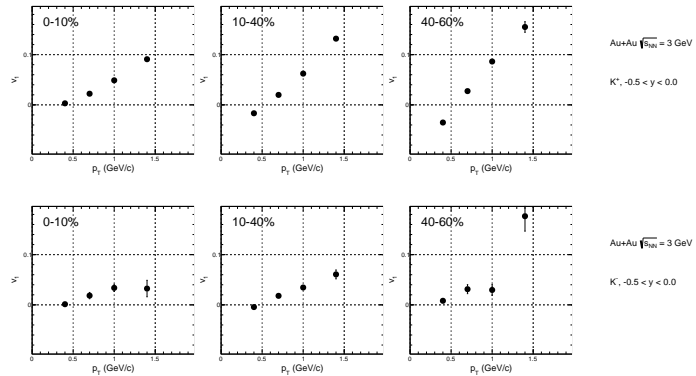


FIG. 24. kaons' v_1 as a function of transverse momentum (p_T) in Au+Au collisions at $\sqrt{s_{NN}} = 3$ GeV in 0-10%, 10-40% and 40-60% centrality bins.

242 3.1.3. *proton v_1 as a function of p_T and rapidity*

243 In this subsection, we will show the results of proton v_1 as a function of p_T and rapidity(y).
 244 Figure 25 shows proton v_1 as a function of y for different centrality bins from 0-5% to 50-60%,
 245 The red line is fitting function 24, p_T range is [0.4, 2.0] GeV/c, which is same with STAR BES-I
 246 results. As we can see, the magnitude of proton's v_1 has centrality dependence, figure ?? shows
 247 proton dv_1/dy as a function of centrality. In order to make comparison to STAR BES-I results, we
 248 have these results in wider centrality bin in the figure 27. And the v_1 slope has maximum value in
 249 the mid-central collision.

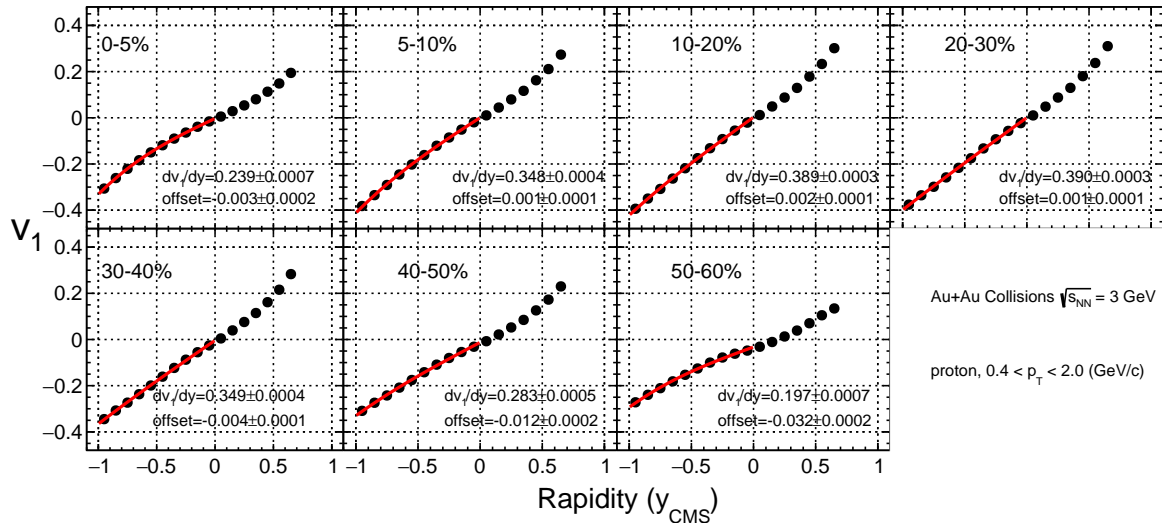


FIG. 25. v_1 as a function of rapidity(y) in different centrality bins for proton in Au+Au collisions at $\sqrt{s_{NN}}$. The red line is fitting function.

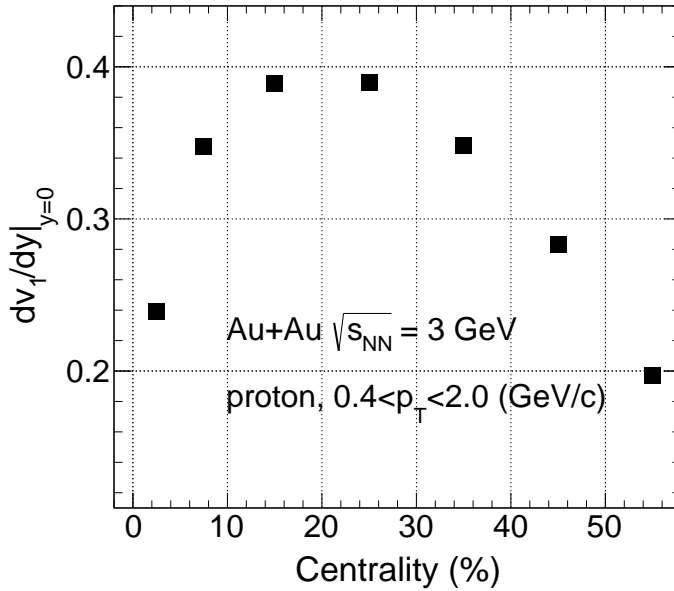


FIG. 26. protons' v_1 slope dv_1/dy as a function of centrality in Au+Au collisions $\sqrt{s_{NN}} = 3 \text{ GeV}$.

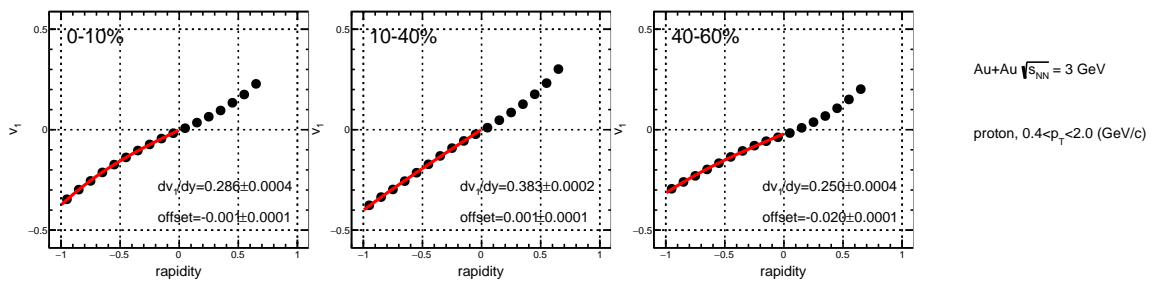


FIG. 27. protons' v_1 as a function of rapidity (y) in Au+Au collision at $\sqrt{s_{NN}} = 3 \text{ GeV}$ in 0-10%, 10-40% and 40-60% bins.

250 We also study the p_T dependence of protons' v_1 in the mid-rapidity region ($-0.5 < y < 0$) in dif-
 251 ferent centrality bins in the figure 28. As we can see, protons v_1 is increasing with p_T increasing.
 252 Figure 29 also shows the results in the wider centrality bins. Since we do see the clear p_T and
 253 rapidity dependence for proton v_1 and we have fruitful statistics for proton at 3 GeV, we would
 254 like to do the 2D scan for proton v_1 , 1: we scan p_T bins to plot v_1 as a function of rapidity, 2: we
 255 scan rapidity bins to plot v_1 as a function of p_T . As we can see in the figure 30.

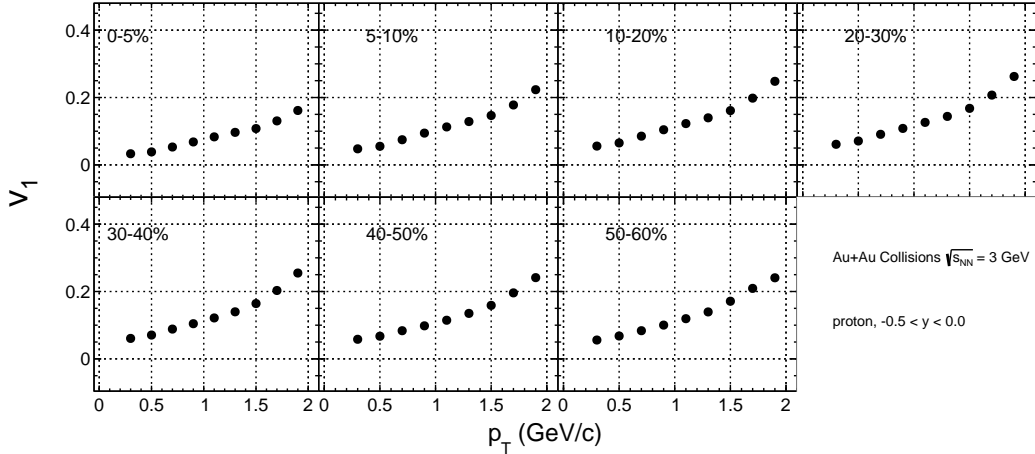


FIG. 28. protons' v_1 as a function of transverse momentum (p_T) in Au+Au collisions at $\sqrt{s_{NN}} = 3$ GeV.

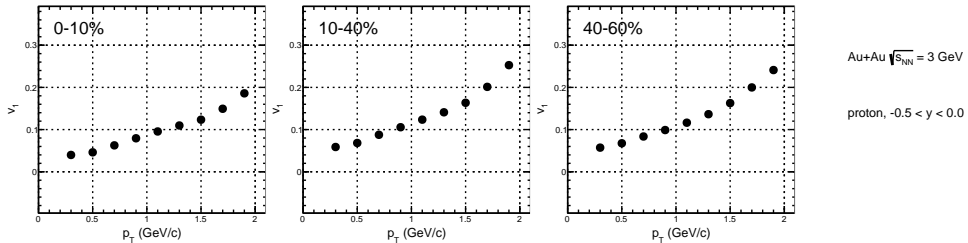


FIG. 29. protons' v_1 as a function of transverse momentum (p_T) in Au+Au collisions at $\sqrt{s_{NN}} = 3$ GeV in 0-10%, 10-40% and 40-60% centrality bins.

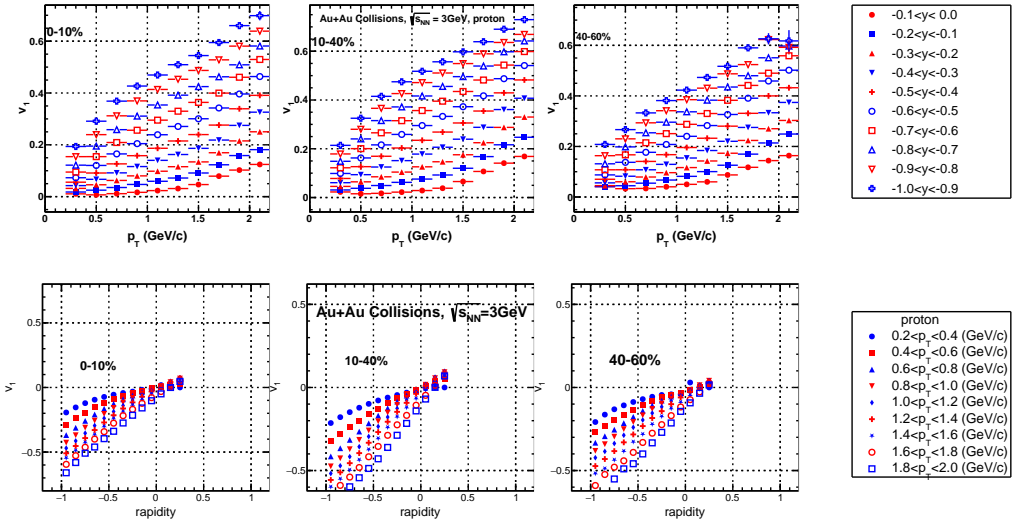


FIG. 30. protons' v_1 as a function of p_T in fine rapidity bins and as a function of rapidity in fine p_T bins in 0-10%, 10-40% and 40-60% at $\sqrt{s_{NN}} = 3\text{ GeV}$.

256 **3.2. v_2 results for π, K, p**

257 In this sub-section, we will show the v_2 as a function of p_T and rapidity(y) in fine centrality
 258 bins for π^\pm, K^\pm and proton. It is expected to have a negative v_2 value at mid-rapidity region based
 259 on world data due to the "squeeze-out" effect when the center of mass energy is below 4 GeV. This
 260 is because at such low energy, the passage time of projectile and target spectators is comparable or
 261 larger than the expansion time QGP medium, thus the spectators will shadow or squeeze out the
 262 medium expansion in the impact parameter direction, which will result in the out-of plane v_2 , the
 263 negative v_2 value.

264 **3.2.1. pions v_2 as a function of p_T and rapidity**

265 In this subsection, we will show the results of pions' v_2 as a function of p_T and rapidity(y).
 266 Figure 31 shows pion v_2 as a function of y for different centrality bins from 0-5% to 50-60%.
 267 The p_T range is [0.2, 1.6] GeV/c. As we can see, we have observed the negative pion v_2 value at
 268 mid-rapidity region, and it has weak rapidity dependence for both π^+ and π^- . Which we do see the
 269 difference between π^+ and $\pi^- v_2$, $\pi^- v_2$ is a little larger than $\pi^+ v_2$. In the BES-I flow results, we
 270 also see the difference between π^+ and $\pi^- v_2$, which has been interpreted by the isospin effect or
 271 mean-filed potential effect. Figure 32 shows the pions' v_2 vs. y in wider centrality bin.

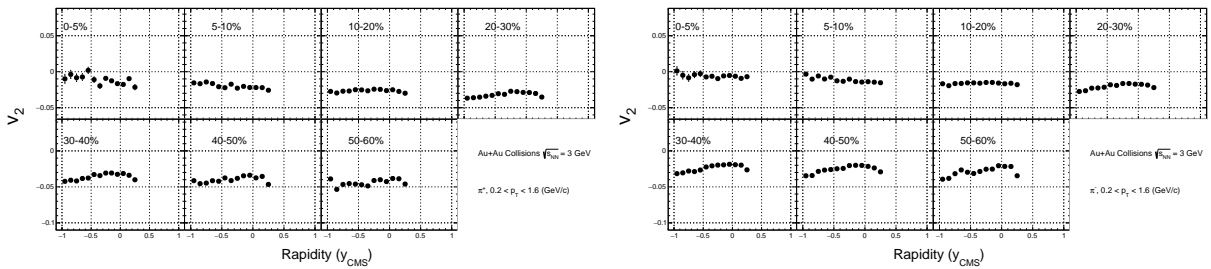


FIG. 31. v_2 as a function of rapidity(y) in different centrality bins for π^+ and π^- in Au+Au collisions at $\sqrt{s_{NN}} = 3$ GeV.

272 We also study the p_T dependence for pions' v_2 in the figure 33, as we can see, pions' v_2 is
 273 decreasing with p_T increasing. Figure 34 shows these results in wider centrality bins 0-10%,
 274 10-40%, 40-60%.

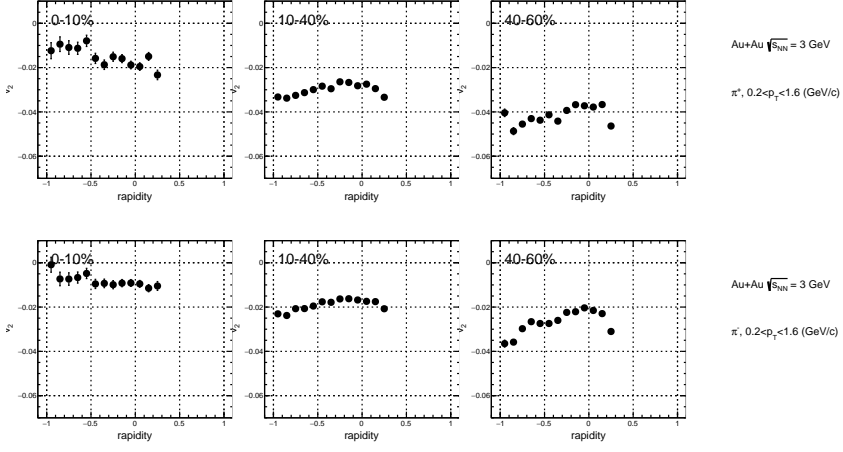


FIG. 32. v_2 as a function of rapidity(y) in different centrality bins for π^+ and π^- in Au+Au collisions at $\sqrt{s_{NN}} = 3$ GeV in 0-10%, 10-40%, 40-60% centrality bins.

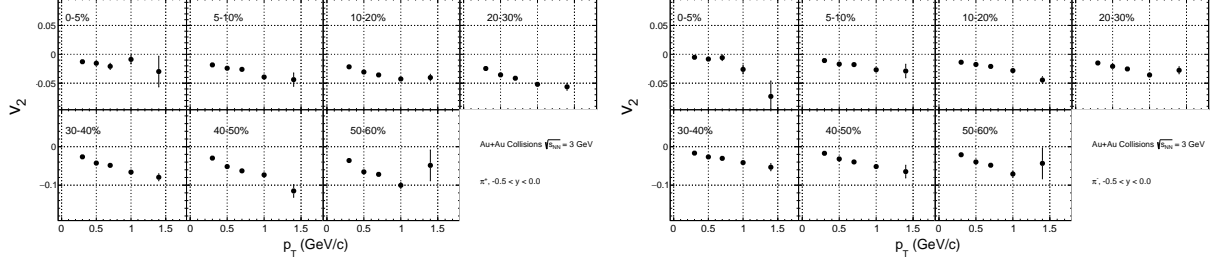


FIG. 33. v_2 as a function of p_T in different centrality bins for π^+ and π^- in Au+Au collisions at $\sqrt{s_{NN}} = 3$ GeV.

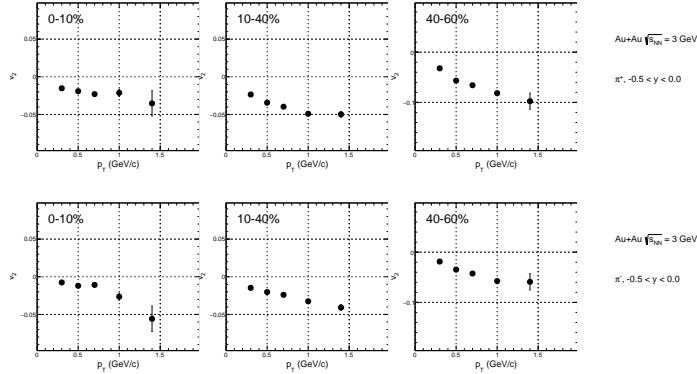


FIG. 34. v_2 as a function of p_T in different centrality bins for π^+ and π^- in Au+Au collisions at $\sqrt{s_{NN}} = 3$ GeV in 0-10%, 10-40%, 40-60% centrality bins.

275 3.2.2. *kaons v_2 as a function of p_T and rapidity(y)*

276 In this subsection, we will show the results of kaons' v_2 as a function of p_T and rapidity(y).
 277 Figure 35 shows kaon v_2 as a function of y for different centrality bins from 0-5% to 50-60%. The
 278 p_T range is [0.4, 1.6] GeV/c. Figure 36 shows the kaons' v_2 vs. y in wider centrality bin. K^+ and
 279 $K^- v_2$ are consistent within error bar.

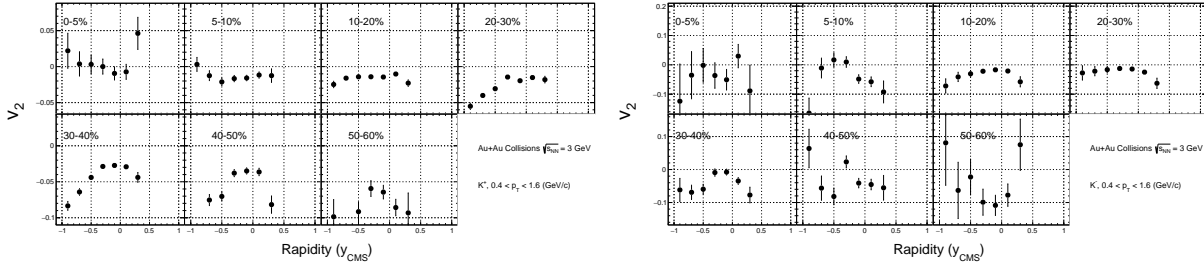


FIG. 35. v_2 as a function of rapidity(y) in different centrality bins for K^+ and K^- in Au+Au collisions at $\sqrt{s_{NN}} = 3$ GeV.

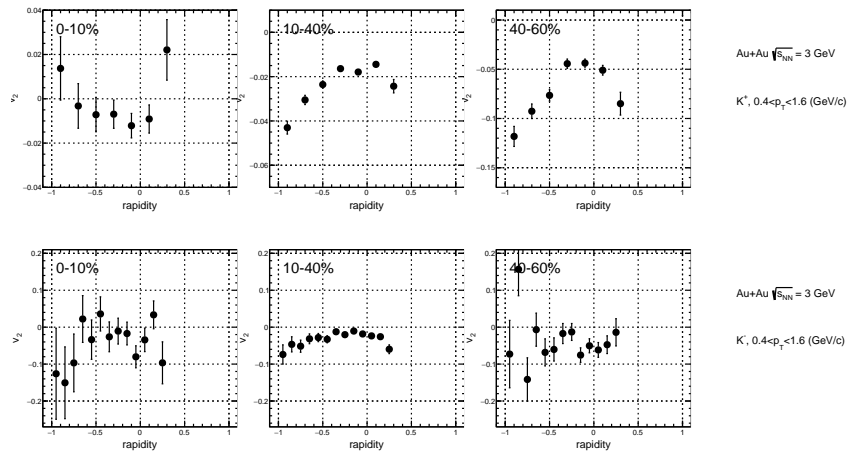


FIG. 36. v_2 as a function of rapidity(y) in different centrality bins for K^+ and K^- in Au+Au collisions at $\sqrt{s_{NN}} = 3$ GeV in 0-10%, 10-40%, 40-60% centrality bins.

280 We also study the p_T dependence for kaons' v_2 in the figure 37, as we can see, kaons' v_2
 281 is decreasing with p_T increasing. Figure 38 shows these results in wider centrality bins 0-10%,
 282 10-40%, 40-60%.

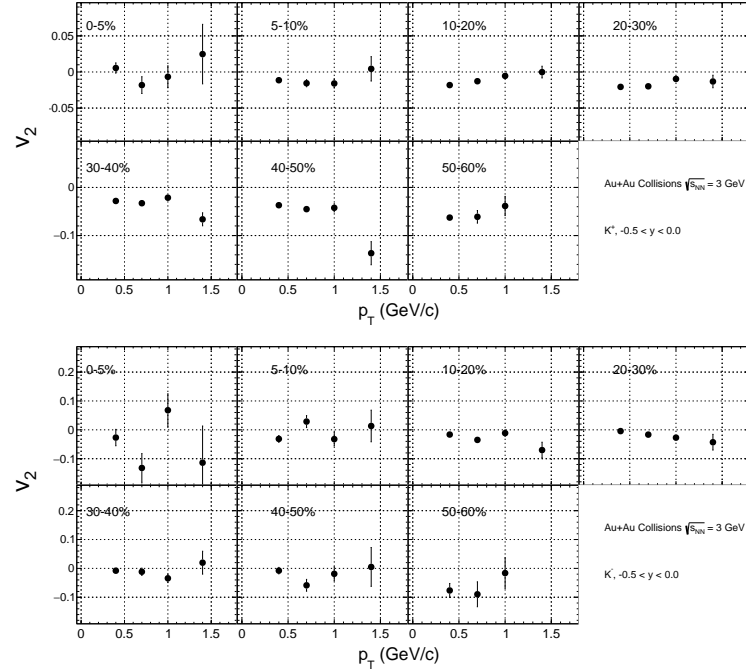


FIG. 37. v_2 as a function of p_T in different centrality bins for K^+ and K^- in Au+Au collisions at $\sqrt{s_{NN}} = 3$ GeV.

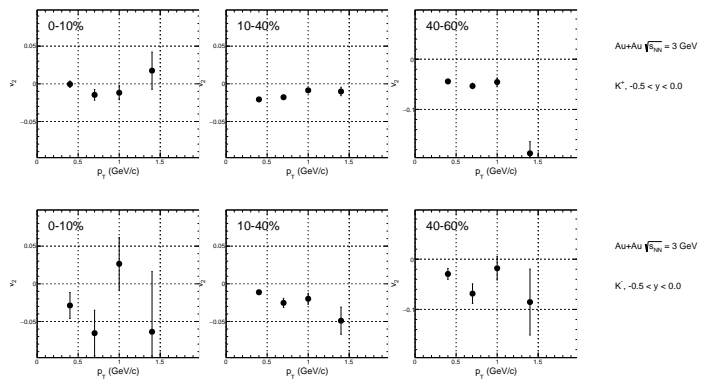


FIG. 38. v_2 as a function of p_T in different centrality bins for K^+ and K^- in Au+Au collisions at $\sqrt{s_{NN}} = 3$ GeV in 0-10%, 10-40%, 40-60% centrality bins.

283 **3.2.3. proton v_2 as a function of p_T and rapidity**

284 In this subsection, we will show the results of protons' v_2 as a function of p_T and rapidity(y).
 285 Figure 39 shows proton v_2 as a function of y for different centrality bins from 0-5% to 50-60%.
 286 The p_T range is [0.4, 2.0] GeV/c. Figure 40 shows the proton's v_2 vs. y in wider centrality bin.
 287 As we can see, proton v_2 is negative at mid-rapidity region. In 0-10% and 10-40% centrality bin,
 288 proton v_2 is negative at mid-rapidity region, while is positive at forward rapidity region.

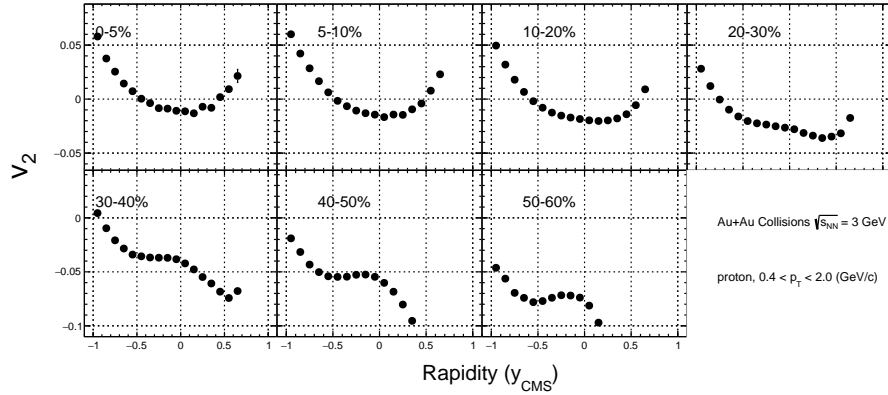


FIG. 39. proton v_2 as a function of rapidity(y) in different centrality bins in Au+Au collisions at $\sqrt{s_{\text{NN}}} = 3$ GeV.

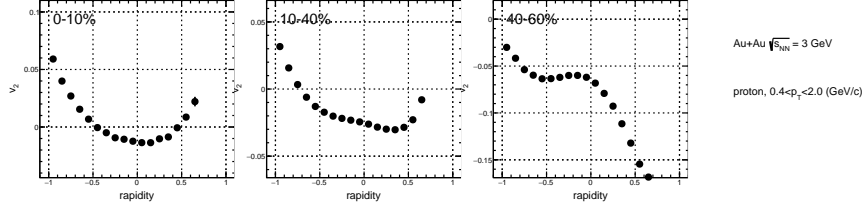


FIG. 40. proton v_2 as a function of rapidity(y) in different centrality bins for in Au+Au collisions at $\sqrt{s_{\text{NN}}} = 3 \text{ GeV}$ in 0-10%, 10-40%, 40-60% centrality bins.

289 We also study the p_T dependence for proton's v_2 in the figure 41, as we can see, proton's v_2
 290 is decreasing with p_T increasing. Figure 42 shows these results in wider centrality bins 0-10%,
 291 10-40%, 40-60%. The proton v_2 decreases with p_T increases, then proton v_2 increases at higher
 292 p_T region.

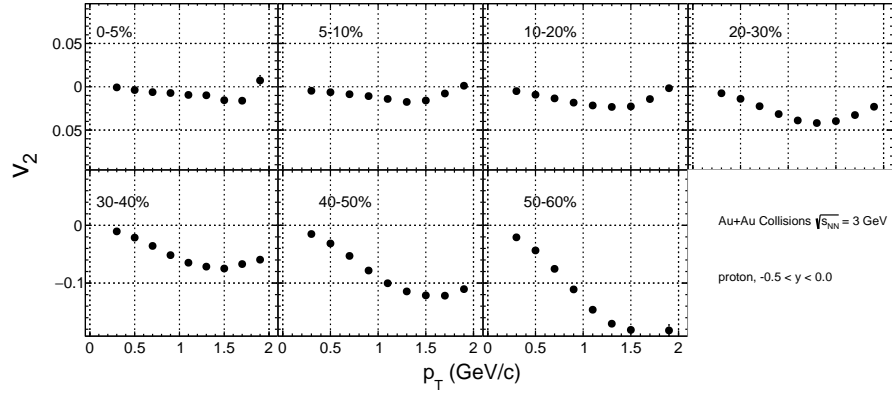


FIG. 41. proton v_2 as a function of p_T in different centrality bins in Au+Au collisions at $\sqrt{s_{NN}} = 3$ GeV.

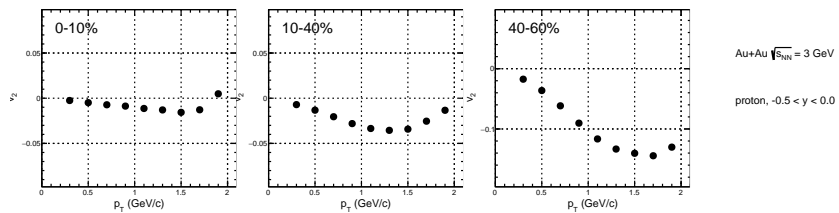


FIG. 42. proton v_2 as a function of p_T in different centrality bins in Au+Au collisions at $\sqrt{s_{NN}} = 3$ GeV in 0-10%, 10-40%, 40-60% centrality bins.

293 **3.3. v_2 from second order event plane**

294 As discussed in the second section, the v_2 is calculated from first order event plane angle Ψ_1 , this
 295 is because the higher first order event plane resolution (up to 70%) than second order resolution,
 296 which will induce the higher lower error bar for v_2 , and numerically it is equivalent to that we
 297 use second order event plane angle Ψ_2 to calculate v_2 . The different order event plane resolution
 298 comparison can be found in the figure 43. Here in the figure 44, we show the reconstructed second
 299 order event plane angle distribution in different centrality in different sub-event group of TPC
 300 and EPD. The black line is raw Ψ_2 distribution, the blue line is Ψ_2 distribution with re-centering
 301 calibration and red line is Ψ_2 distribution with re-centering and shift calibration, as we can see,
 302 after re-centering and shift calibration (the red line) we have flat second order event plane angle
 303 Ψ_2 distribution, and it can be used for v_2 calculation.

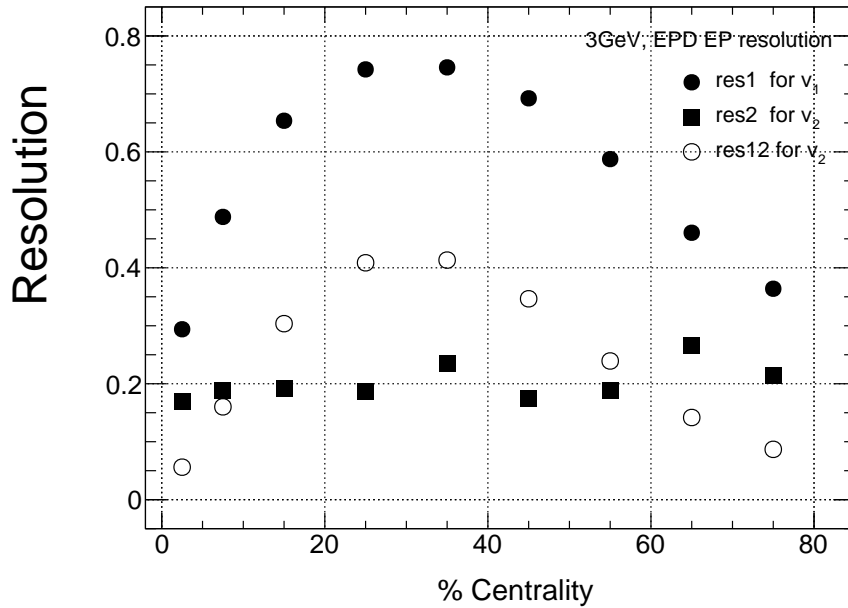


FIG. 43. EPD event plane resolution as a function of collision centrality, the black solid circle is first order event plane resolution, black open circle is the converted second order event plane resolution for v_2 calculation, the black solid square is second order event plane resolution.

304 We calculate the proton v_2 as a function of p_T using second order event plane angle Ψ_2 and
 305 make comparison to the results from using first order event plane angle. It can be found in the
 306 figure 45. We found their results are consistent in the low p_T and middle p_T region. There is little
 307 difference in the high p_T region, we think this could be some effect from proton's purity, and the

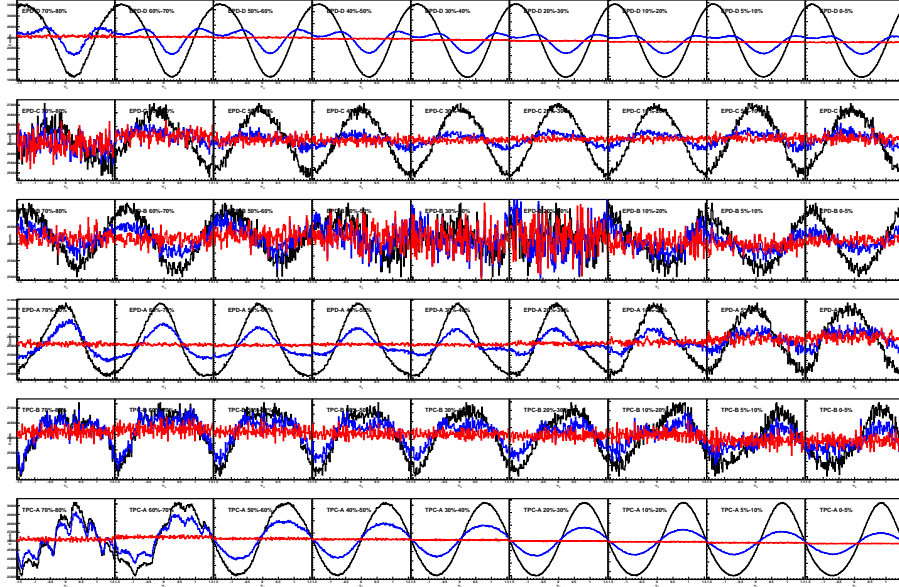


FIG. 44. TPC and EPD sub-event plane angle (Ψ_2) distribution in different centralities, the black line is raw Ψ_2 distribution, the blue line is Ψ_2 distribution with re-centering calibration, the red line is Ψ_2 distribution with re-centering and shift calibration.

308 error is also too large. So far, our conclusion is that the results of v_2 using first order and second
 309 event plane angle are consistent.

310 In order to confirm this, we also do the same analysis (calculate v_2 using first order and second
 311 order event plane angle) using UrQMD model. First, we show the resolution of different order
 312 event plane in the figure ??, we have the same conclusion with data, the second order event plane
 313 resolution is quite small than first order event plane resolution, which will induce larger error bar
 314 when calculating v_2 . In the figure 47, we calculate the v_2 from first order and second event plane
 315 angle and make comparison. We found they are consistent within the error bar.

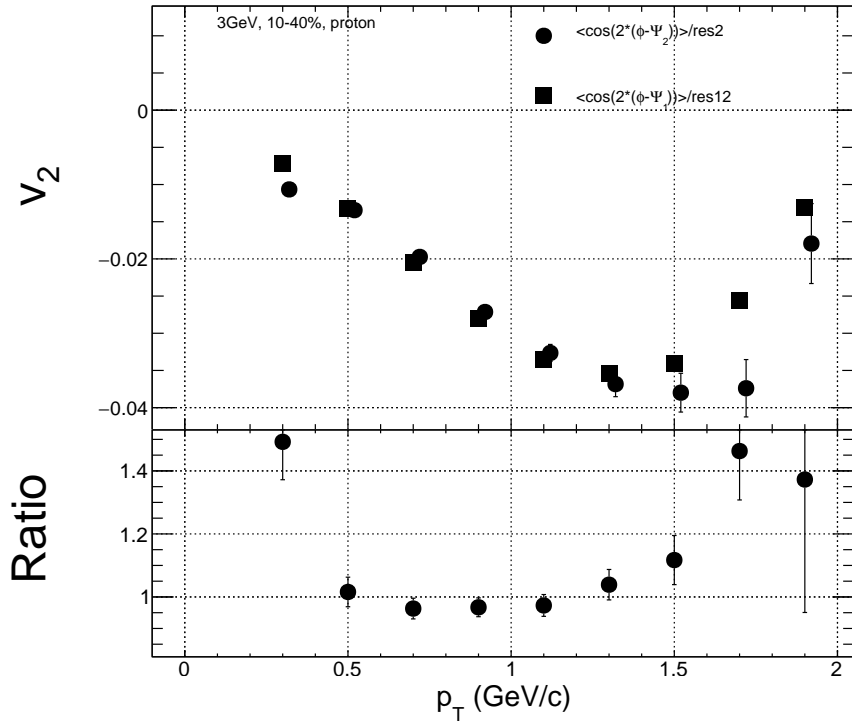


FIG. 45. v_2 as a function of p_T in 3GeV Au+Au collisions, 10-40% centrality from first order and second event plane angle, and their ratio.

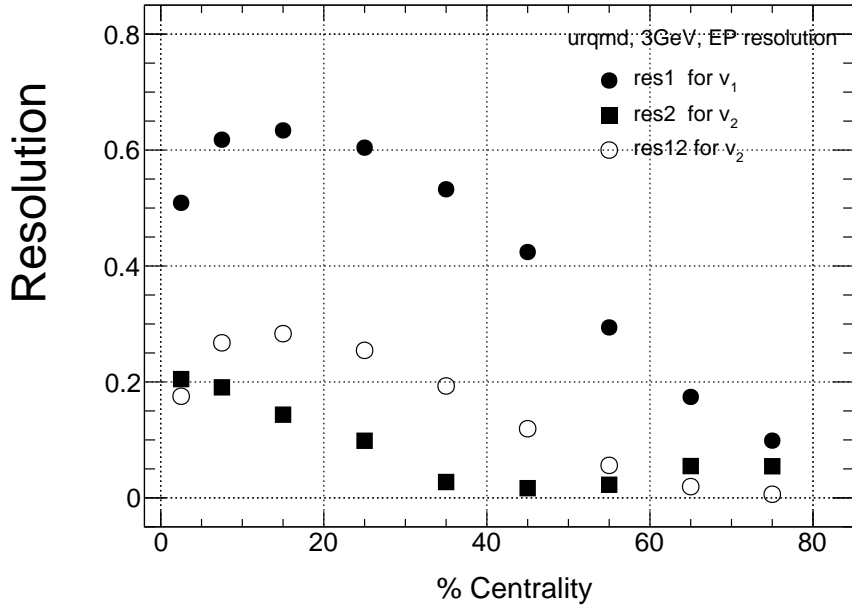


FIG. 46. The event plane resolution as a function collision centrality at 3GeV in UrQMD model for first order second order and converted second order.

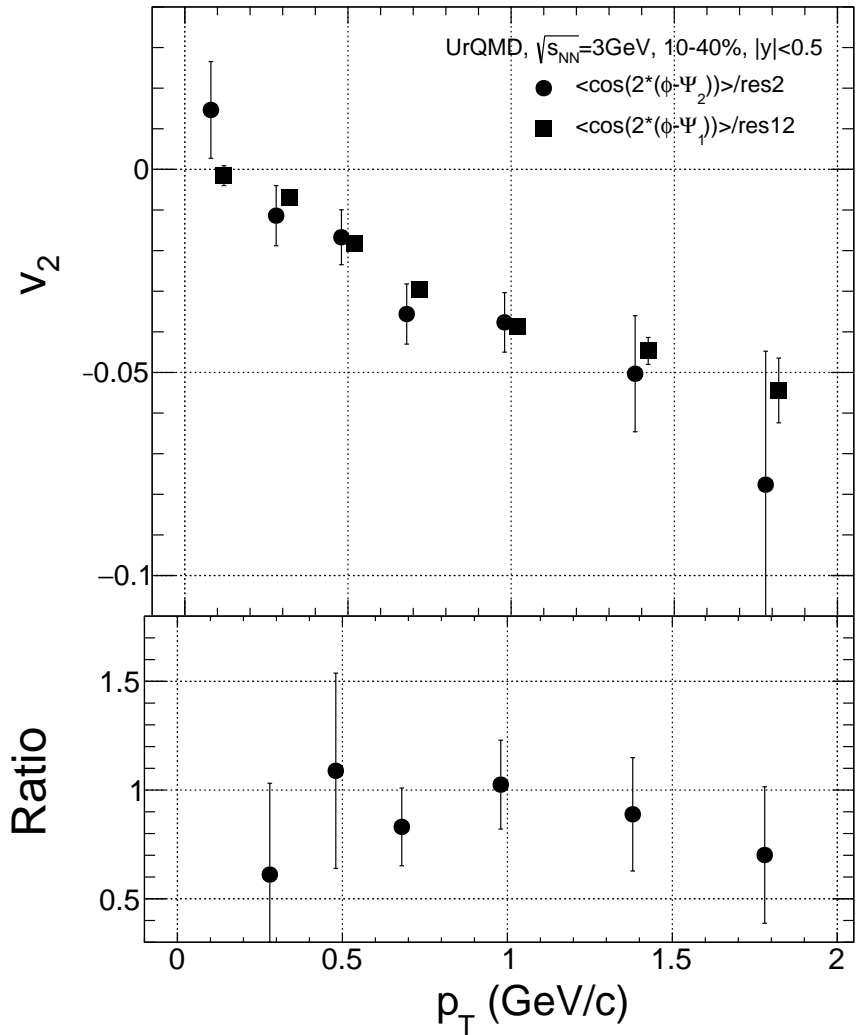


FIG. 47. v_2 as a function of p_T at 3 GeV 10-40% in UrQMD model from first order and second event plane angle, and their ratio.

316 **3.4. Systematic Uncertainties**

317 Point-by-point systematic errors on variables used for tracks cuts and particle identification and
 318 resolution. For all systematic checks, the various cuts are changed one at a time. Table VI shows
 319 the systematic cuts and minimum and maximum values used in the analysis for pions and kaons.
 320 Similarly, table VII shows the systematic cuts used in the analysis for proton. For each cut vari-
 321 able, we choose the maximum deviation from default value, then the total systematic uncertainty
 322 can be estimated using in the equation 23 from different source (dca, nHitsFit, $n\sigma_{particle}$, resolu-
 323 tion, efficiency). The systematic uncertainty contribution from resolution should be constants for
 324 each particle in fine centrality bin. While there will be difference in wide centrality bin(10-40%)
 325 because the relative number of particles in fine centrality bin are not same for each particle species.
 326 But in this analysis, the

$$sys_{total} = \sqrt{(y_{dca} - y_{def})^2 + (y_{nHit} - y_{def})^2 + (y_{n\sigma} - y_{def})^2 + (y_{EP} - y_{def})^2 + (y_{eff} - y_{def})^2} \quad (23)$$

TABLE VI. Systematic cuts for pions and kaons

Cuts	Default	var1	var2
dca (<)	3	1	2
nHitFit (>)	15	10	20
$n\sigma_{particle}$ <	3	2	2.5
resolution reference EP EPD-C EPD-CD EPD D			

TABLE VII. Systematic cuts for proton

Cuts	Default	var1	var2
dca (<)	3	1	2
nHitFit (>)	15	10	20
$n\sigma_{particle}$ <	2	3	2.5
resolution reference EP EPD-C EPD-CD EPD D			

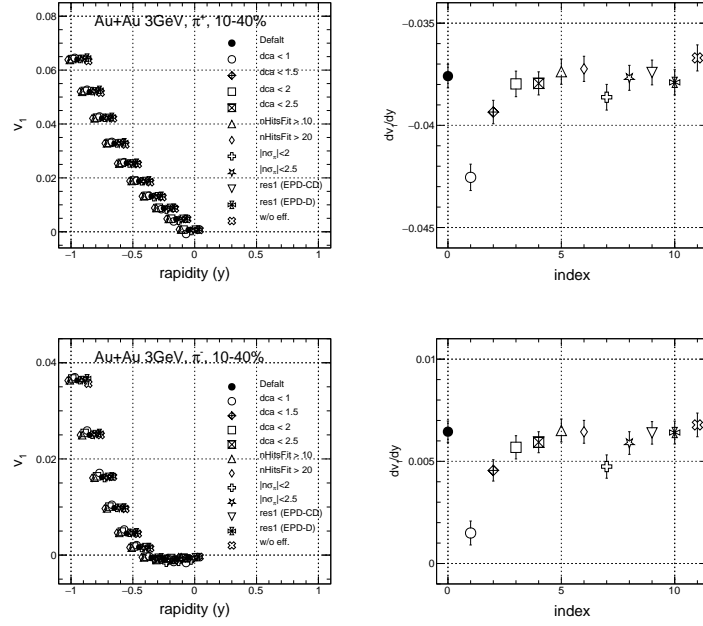


FIG. 48. Systematic uncertainty study for v_1 as a function of rapidity in 10-40% for pion at $\sqrt{s_{NN}} = 3$ GeV. Left is v_1 as a function of rapidity from different cut, right is fitted results of dv_1/dy from different source cut .

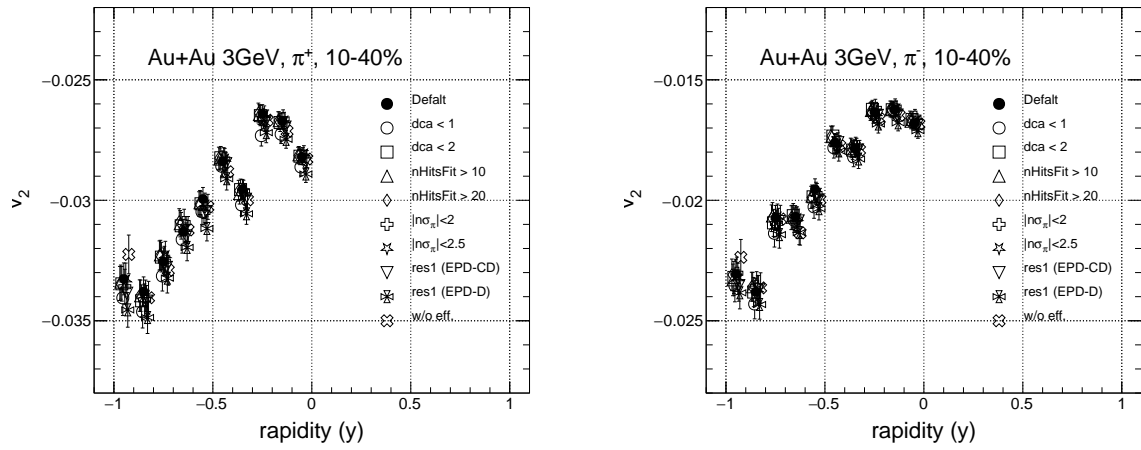


FIG. 49. Systematic uncertainty study for v_2 as a function of rapidity in 10-40% for pion at $\sqrt{s_{NN}} = 3$ GeV.

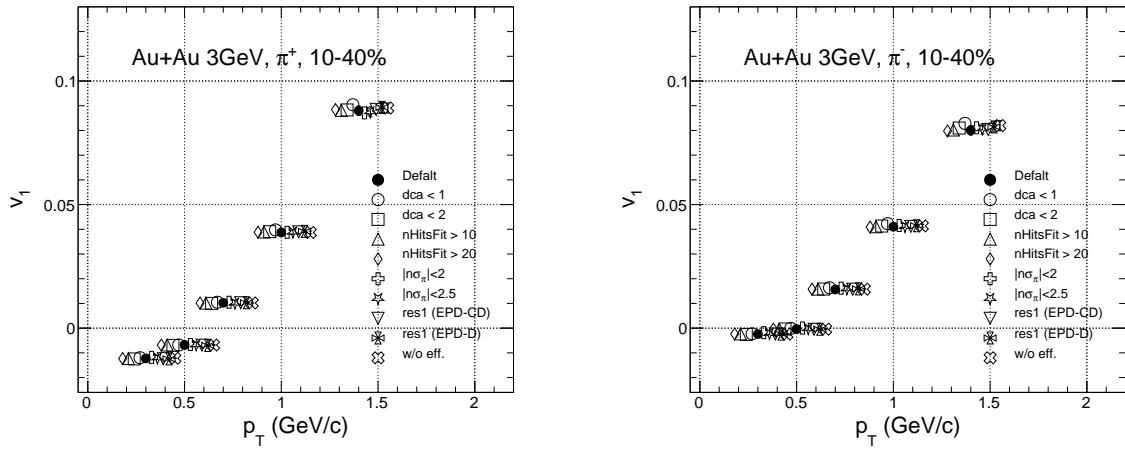


FIG. 50. Systematic uncertainty study for v_1 as a function of p_T in 10-40% for pion at $\sqrt{s_{NN}} = 3$ GeV

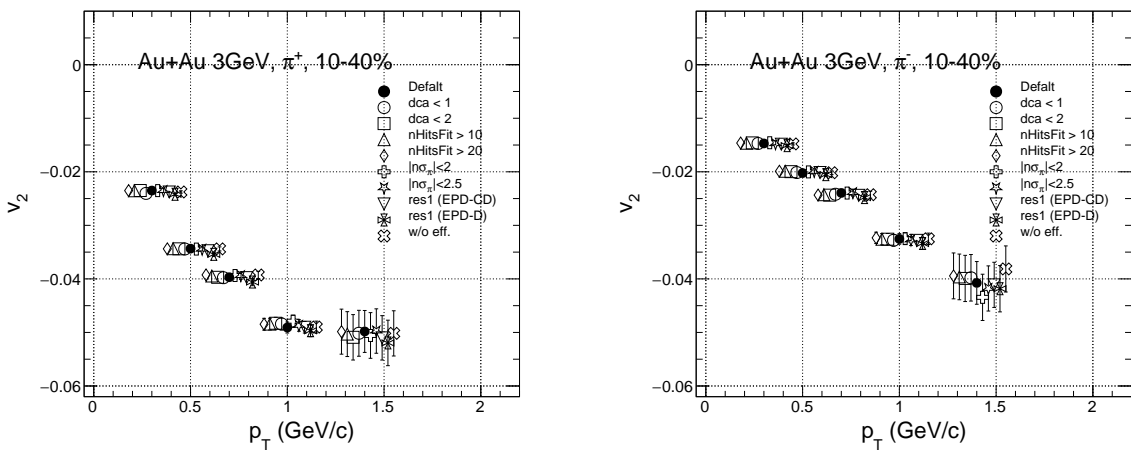


FIG. 51. Systematic uncertainty study for v_2 as a function of p_T in 10-40% for pion at $\sqrt{s_{NN}} = 3$ GeV.

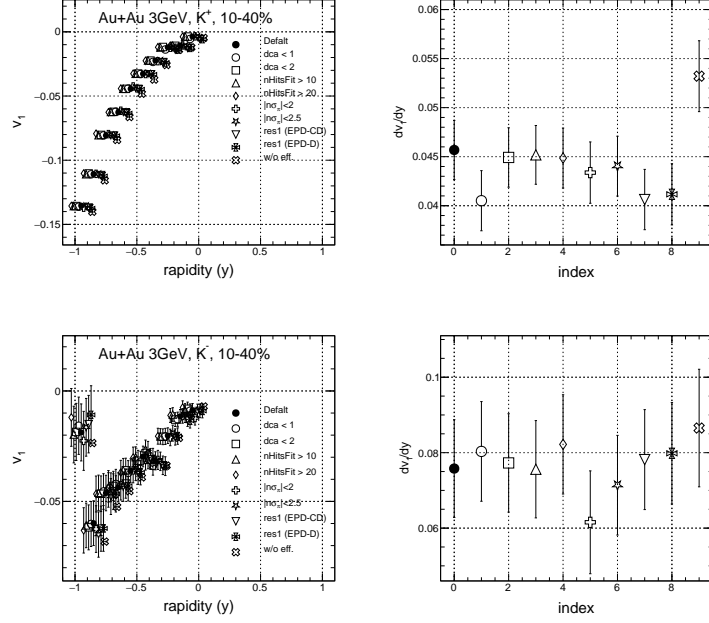


FIG. 52. Systematic uncertainty study for v_1 as a function of rapidity in 10-40% for kaon at $\sqrt{s_{NN}} = 3$ GeV. Left is v_1 as a function of rapidity from different cut, right is fitted results of dv_1/dy from different source cut .

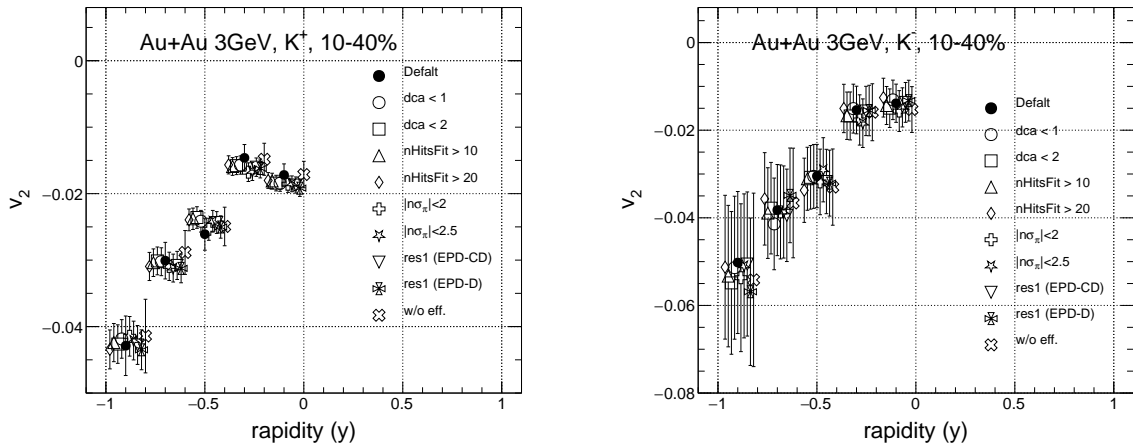


FIG. 53. Systematic uncertainty study for v_2 as a function of rapidity in 10-40% for kaon at $\sqrt{s_{NN}} = 3$ GeV.

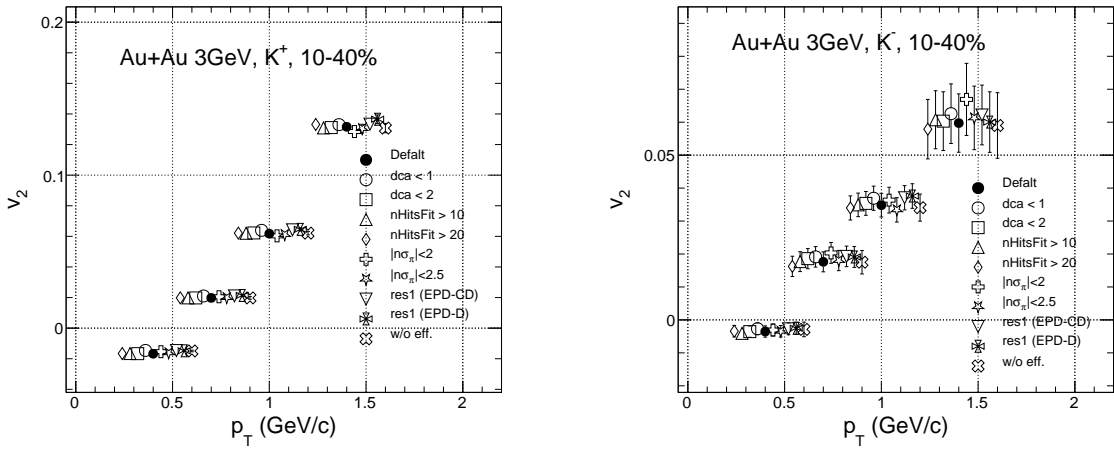


FIG. 54. Systematic uncertainty study for v_1 as a function of p_T in 10-40% for kaon at $\sqrt{s_{NN}} = 3$ GeV

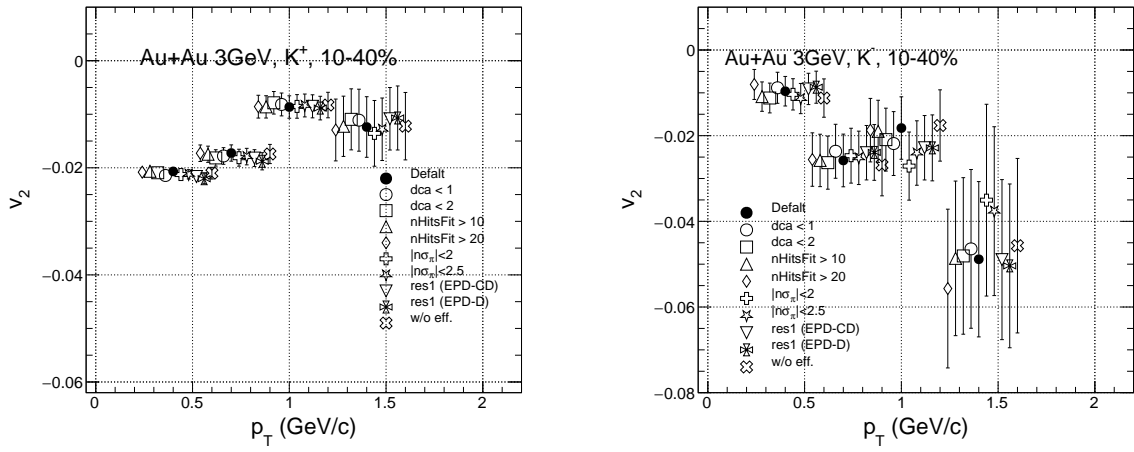


FIG. 55. Systematic uncertainty study for v_2 as a function of p_T in 10-40% for kaon at $\sqrt{s_{NN}} = 3$ GeV.

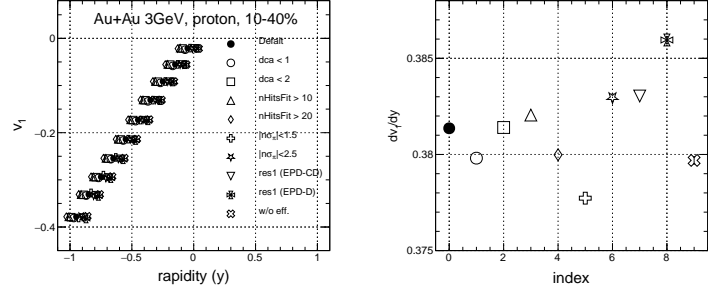


FIG. 56. Systematic uncertainty study for v_1 as a function of rapidity in 10-40% for proton at $\sqrt{s_{NN}} = 3$ GeV. Left is v_1 as a function of rapidity from different cut, right is fitted results of dv_1/dy from different source cut .

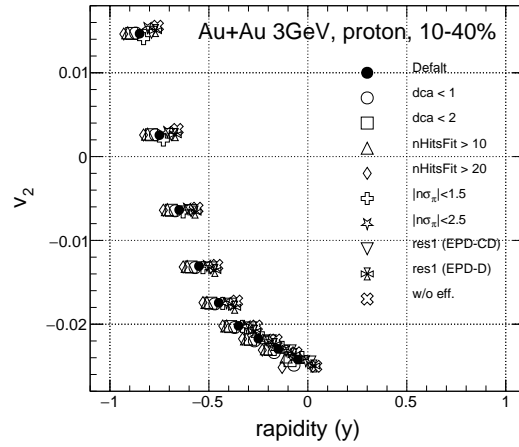


FIG. 57. Systematic uncertainty study for v_2 as a function of rapidity in 10-40% for proton at $\sqrt{s_{NN}} = 3$ GeV.

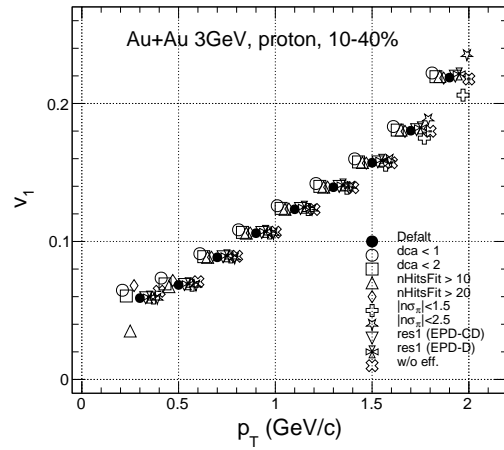


FIG. 58. Systematic uncertainty study for v_1 as a function of p_T in 10-40% for proton at $\sqrt{s_{NN}} = 3$ GeV

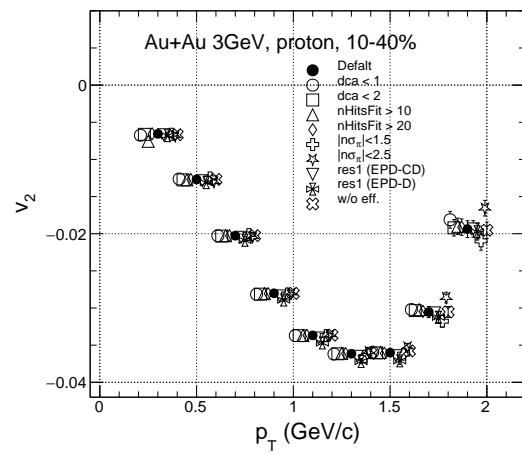


FIG. 59. Systematic uncertainty study for v_2 as a function of p_T in 10-40% for proton at $\sqrt{s_{NN}} = 3$ GeV.

327 **4. DISCUSSION**

328 In this section, we will review the results of number of constituent quark scaling of elliptic for
329 identified particles from STAR BES-I and compare with the results that from 3 GeV to discuss the
330 partonic collectivity at RHIC-STAR energy region. The p_T integrated v_2 will also be discussed
331 and compared with world data. The excitation function indicates the elliptic flow evolves from a
332 in-plane flow ($v_2 > 0$) to an out-of-lane flow pattern as the collision energy decreases. The directed
333 flow slope of identified particle will be discussed and compared with the higher energy from STAR
334 BES-I.

335 **4.1. Number of constituent quark scaling of elliptic flow (v_2)**

336 Quark coalescence [?] and recombination model [?] for heavy-ion collisions predict that if
337 particles are made up of quarks then the elliptic flow $v_2(p_T)$ of the particles will scale with their
338 number of constituent quarks.

$$v_1(y) = F * y + C * y^3 + b \quad (24)$$

339 Where parameter F is the v_1 slop dv_1/dy , parameter C is the fluctuation term and parameter b is
340 the offset to origin point.